

Contents lists available at ScienceDirect

# Journal of the Mechanics and Physics of Solids

journal homepage: www.elsevier.com/locate/jmps





# On the micromechanics of void mediated failure in HCP crystals

Padmeya P. Indurkar a,b, Shailendra P. Joshi b,\*, A. Amine Benzerga c,d,e

- <sup>a</sup> Department of Mechanical Engineering, National University of Singapore, Singapore 117576, Singapore
- <sup>b</sup> Department of Mechanical Engineering, University of Houston, Houston, 77204-4006, United States of America
- <sup>c</sup> Department of Materials Science and Engineering, Texas A & M University, College Station, TX 77843, United States of America
- d Center for Intelligent Multifunctional Materials and Structures, TEES, College Station, TX 77843, United States of America
- e Department of Aerospace Engineering, Texas A & M University, College Station, TX 77843, United States of America

#### ARTICLE INFO

# Keywords: HCP crystal plasticity Void growth and coalescence Void shape effect

#### ABSTRACT

Three-dimensional voided cell calculations are carried out to investigate the effect of initially flat voids on the effective behavior of hexagonal crystals. The crystalline matrix is described using a set of constitutive relations that account for slip and twinning. In some materials, the limiting case of penny-shaped cracks better represents incipient void formation. Cell boundary conditions are such that internal necking of the intervoid ligament or void impingement are the only possible failure modes. The overall behavior of the cell is analyzed under various stress states and two loading orientations, with special attention given to the evolution of damage-relevant microstructural variables. Particular emphasis is placed on crystallographic aspects of void growth and coalescence, which often prove difficult to represent using phenomenological anisotropic plasticity models.

# 1. Introduction

Hexagonal close-packed (HCP) alloys are promising candidates for a range of applications (Mordike and Ebert, 2001), notably in transportation (Friedrich and Schumann, 2001) and health industries (Zhang et al., 2009). Extensive work has been conducted on modeling the thermodynamics and kinetics of anisotropic plastic flow by virtue of low crystallographic symmetry in HCP metals and twinning induced tension–compression asymmetry. Such work includes phenomenological single crystal plasticity (Kalidindi, 1998; Zhang and Joshi, 2012); viscoplastic self-consistent modeling (Agnew et al., 2006; Beyerlein and Tomé, 2008), with enhanced physical features including twinning–detwinning (Wang et al., 2012) and twinning nucleation and propagation (Cheng and Ghosh, 2017); models with reduced crystallographic features (Becker and Lloyd, 2016) as well as simpler, reduced-order models employing single (Plunkett et al., 2008) or multiple (Lee et al., 2008; Kondori et al., 2019) yield surfaces. This segment of the literature is concerned with damage-free plasticity in HCP materials. It is far from sufficient in implementing damage tolerance assessment procedures for critical applications.

Experimental work on damage and failure characterization in structural materials, such as Mg alloys, initially focused on simple stress states (e.g., uniaxial loading) (Barnett, 2007a,b). Some authors explored other stress states using rectangular notched or precracked specimens (Al-Samman and Gottstein, 2008; Somekawa et al., 2009; Steglich and Morgeneyer, 2013; Kaushik et al., 2014). However, in rectangular bars failure is often instability-driven. In these experiments, damage was typically localized and this led to de-emphasizing the usual progressive damage accumulation mechanisms observed in metals (Pineau et al., 2016) in subsequent modeling efforts.

E-mail address: shailendra@uh.edu (S.P. Joshi).

<sup>\*</sup> Corresponding author.

Kondori and Benzerga (2014) deformed round notched bars of a Mg alloy to fracture and showed evidence of internal damage accumulation through void nucleation, growth and coalescence. Furthermore, by varying the notch acuity, they showed a decreasing strain to failure with increasing stress triaxiality. Such trends were later confirmed using high-resolution tomography (Kondori et al., 2018) as well as for other alloys, e.g., Kondori and Benzerga (2015), Prasad et al. (2018) and high-rate loadings, e.g., Kale et al. (2018). Use of cylindrical notched specimens reduces the propensity for shear localization, induces a damage zone in the notch, and thus enables probing damage accumulation under multi-axial stress states. Void nucleation occurs by cracking of second-phase particles (Kondori and Benzerga, 2014; Lugo et al., 2011; Bhattacharyya et al., 2017) or due to twinning induced micro-crack formation (Koike, 2005; Barnett, 2007b; Bhattacharyya et al., 2017).

The experiments of Kondori and Benzerga (2014) also uncovered an apparent notch-enhanced ductility due to a multi-axial stress state in the notch. This trend was attributed to the activation of additional plasticity mechanisms absent under uniaxial tension. This and subsequent analyses (Selvarajou et al., 2016, 2017) emphasize that the interaction of stress state and microstructure plays a crucial role in plastic deformation and damage tolerance in HCP alloys.

When void growth mechanisms are probed in some detail, two things become apparent. Due to nucleation mechanisms, damage initiates as flat voids, a term that includes twin-induced crack-like defects. In addition, the rate of blunting of the flat voids is much slower than predicted using continuum plasticity for the surrounding matrix, even when anisotropy is considered (Keralavarma et al., 2011). Qualitative and quantitative information about void statistics may be found in the *ex situ* synchrotron tomography studies by Kondori et al. (2018); also see Kondori and Benzerga (2017) for WE43 Mg alloy. What is of particular importance is that although the reduced blunting of flat voids implies reduced rates of net (volumetric) void growth, it does lead to a decrease in ductility, either because their lateral growth reduces intervoid ligament thereby favoring coalescence (Kondori and Benzerga, 2017), or because local cleavage occurs.

The aim of this paper is to carry out an analysis of growth of flat voids in an HCP matrix by means of finite deformation crystal plasticity finite element simulations. In doing so, crystallographic aspects of void growth are considered beyond the net plastic anisotropy of previous analyses (Benzerga and Besson, 2001; Keralavarma et al., 2011). The analyses expand upon previous unit cell simulations in crystal matrices with cubic symmetry, e.g., Potirniche et al. (2006), Ha and Kim (2010), Yerra et al. (2010), Srivastava and Needleman (2013, 2015). More recent investigations elucidate the role of twinning in void-mediated failure (Prasad et al., 2016; Selvarajou et al., 2019; Joshi and Joshi, 2022). In addition to aspects related to reduced void blunting, this type of analysis is needed in guiding the development of homogenization-based porous crystal plasticity. Early effort in this direction goes back to Hori and Nemat-Nasser (1988) who investigated void growth under axisymmetric stress states in face-centered-cubic (FCC) and body-centered cubic (BCC) porous single crystals using an Eshelby inclusion approach. Kysar and co-workers used slip line theory to derive exact stress fields under plane strain for FCC (Kysar et al., 2005) and HCP (Gan and Kysar, 2007) crystals. Han et al. (2013) and Ling et al. (2016) employed a variational principle to obtain Gurson-like yield functions for FCC single crystals. Paux and coworkers (Paux et al., 2015, 2018) extended these formulations to FCC and HCP crystals accounting for material hardening. Mbiakop et al. (2015a,b) developed a modified variational porous plasticity model accounting for void shape effects in FCC, BCC, or HCP single crystals. Recently, Song and Castañeda (2017a) have incorporated void shape evolution within their variational formulation of porous plasticity based on a fully optimized second order approach combined with an iterative homogenization approach. Even more recently, Yang and Ghosh (2022) presented an efficient computational implementation of the yield functions proposed by Han et al. (2013) and Ling et al. (2016) with extension to HCP single crystals. However, none of these formulations account for twinning. The analyses here follow along the lines of Selvarajou et al. (2019) where attention was restricted to initially spherical voids, which are rarely observed in HCP alloys at incipient void formation.

The paper is organized as follows. Section 2 describes the unit-cell setup and the HCP crystal plasticity model. Section 3 presents results for prismatic loading (Section 3.1) and  $\langle c \rangle$ -axis loading (Section 3.2). Section 4 summarizes key findings with emphasis on broader experimental correlations and potential implications. Throughout, second-order and fourth-order tensors are respectively denoted by bold and double-stroke symbols, e.g., **I** and  $\mathbb{I}$ ; the contracted product between  $\mathbb{A}$  and **B** is given by  $\mathbb{A}$ :  $\mathbf{B} = A_{ijkl}B_{kl}$ , the inner product as  $\mathbf{AB} = A_{ik}B_{kj}$ , and dyadic product as  $\mathbf{A} \otimes \mathbf{B} = A_{ij}B_{kl}$ . Similarly, given vectors **a** and **b**, we have  $\mathbf{a} \otimes \mathbf{b} = a_ib_j$ , and  $\mathbf{a} \cdot \mathbf{b} = a_jb_i$ .

#### 2. Formulation

A cubic unit cell with fully periodic kinematic boundary conditions is considered which contains an initially oblate void, Fig. 1. In a global frame  $[\mathbf{e}_x, \mathbf{e}_y, \mathbf{e}_z]$ , the current cell dimensions are denoted  $L_x$ ,  $L_y$ ,  $L_z$  and the current void radii are  $r_x$ ,  $r_y$ ,  $r_z$  with subscript 0 for initial values. The void axis is parallel to the *y*-axis. The cell is discretized using ~60,000 fully integrated linear hexahedral (C3D8) elements in ABAQUS/STANDARD<sup>®</sup>.

The cell geometry is determined by the void volume fraction (or porosity)  $f_0=(4/3)\pi r_{x0}r_{z0}r_{y0}/L_0^3$ , the void aspect ratio  $W_0=r_{y0}/r_{x0}$  (recall that  $r_{x0}=r_{z0}$  for an oblate void) and the cell aspect ratio  $\lambda_0=L_{y0}/L_{x0}$ . An additional parameter of interest is the ligament parameter  $\chi_0=2r_{x0}/L_{x0}=2r_{z0}/L_{z0}$ . The corresponding current values are  $f,W,\lambda$  and  $\chi$ . The deformed void is not axially symmetric. To account for this, an index is introduced where needed, e.g.,  $W_x=r_y/r_x$  and  $\chi_z=r_z/L_z$ .

Overall measures of stress and strain are defined over the unit cell volume V as:

$$\Sigma_{ij} = \frac{1}{V} \int_{V} \sigma_{ij} \, dV \qquad \qquad E_{xx} = \ln\left(\frac{L_x}{L_{x0}}\right); \quad E_{yy} = \ln\left(\frac{L_y}{L_{y0}}\right); \quad E_{zz} = \ln\left(\frac{L_z}{L_{z0}}\right); \tag{1}$$

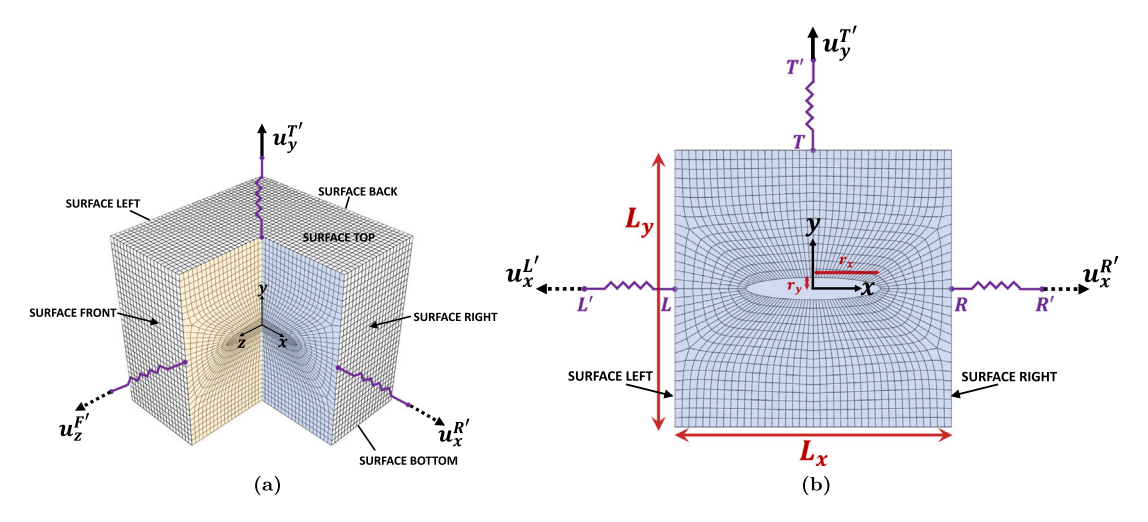


Fig. 1. The unit cell with key dimensions and loading setup (a) Typical finite element mesh (here for  $W_0 = 1/6$ ). (b) Section in central xy-plane.

where  $\sigma_{ij}$  are the components of the Cauchy stress,  $\sigma$ . The mean stress,  $\Sigma_m$ , von Mises equivalent stress,  $\Sigma_{eq}$ , and corresponding equivalent strain,  $E_{ea}$ , are then:

$$\Sigma_{m} = \frac{1}{3}\Sigma : \mathbf{I}; \qquad \Sigma_{eq} = \sqrt{\frac{3}{2}\Sigma' : \Sigma'}; \qquad \Sigma' = \mathbb{J} : \Sigma; \qquad \mathbf{E}_{eq} = \sqrt{\frac{2}{3}\mathbf{E}' : \mathbf{E}'}$$
 (2)

with  $\mathbb{J} = \mathbb{I} - (1/3)\mathbf{I} \otimes \mathbf{I}$  the deviatoric projection tensor. Here, the overall stress state is characterized using the triaxiality ratio  $\mathcal{T} = \Sigma_{\mathrm{m}}/\Sigma_{\mathrm{eq}}$  with  $\Sigma_{vv} \geq \Sigma_{xx} = \Sigma_{zz}$ .

To maintain constant triaxiality, the method of Tekoglu et al. (2012) is used. Five pairs of dummy nodes are added to each face of the unit cell: top (T, T'), right (R, R'), left (L, L'), front (F, F') and back (B, B'). These dummy node pairs are connected using linear spring elements of stiffness k. A displacement  $u_y^{T'}$  is prescribed at T' such that a constant engineering strain rate of  $1 \times 10^{-3}$  s<sup>-1</sup> is applied along the y direction. The resulting displacements  $u_x^{R'}$ ,  $u_x^{L'}$ ,  $u_z^{F'}$ ,  $u_z^{B'}$  are iteratively calculated using a multi-point constraint algorithm, such that the force transferred through the respective spring elements to the unit cell results in a constant value of T. Kinematic periodicity is ensured by adding the following constraint equations

$$u_y^{n,\mathrm{top}} - u_y^{n,\mathrm{bottom}} = u_y^{\mathrm{T}} - u_y^{\mathrm{B}} \quad ; \quad u_x^{n,\mathrm{right}} - u_x^{n,\mathrm{left}} = u_x^{\mathrm{R}} - u_x^{\mathrm{L}} \quad ; \quad u_z^{n,\mathrm{front}} - u_z^{n,\mathrm{back}} = u_z^{\mathrm{F}} - u_z^{\mathrm{E}}$$

for all nodes n on the face. To avoid rigid body motions, the central node of the bottom face is pinned (i.e.,  $u_y^B = 0$ ). Further details can be found in Tekoglu et al. (2012) and Indurkar (2020).

A finite-strain crystal plasticity formulation is adopted to describe the rate-dependent behavior of the matrix material. The formulation follows that of Zhang and Joshi (2012), as employed in previous studies (Selvarajou et al., 2016, 2019). It is based on the multiplicative decomposition of deformation gradient  $\mathbf{F}$  into an elastic part,  $\mathbf{F}^e$ , and a plastic part,  $\mathbf{F}^p$ . The velocity gradient is then  $\mathbf{L} = \dot{\mathbf{F}}\mathbf{F}^{-1} = \mathbf{L}^e + \mathbf{L}^p$  with:

$$\mathbf{L}^{p} = \mathbf{F}^{e} \dot{\mathbf{F}}^{p} \mathbf{F}^{p-1} \mathbf{F}^{e-1} \tag{3}$$

where a dot stands for the material derivative. The plastic part,  $L^p$ , is given in the current configuration as the sum of slip and twinning contributions:

$$\mathbf{L}^{p} = \underbrace{\left(1 - \sum_{\beta=1}^{N_{\text{tw}}} \phi^{\beta}\right) \sum_{\alpha=1}^{N_{s}} \dot{\gamma}^{\alpha} (\mathbf{s}^{\alpha} \otimes \mathbf{m}^{\alpha})}_{\text{slip in parent}} + \underbrace{\sum_{\beta=1}^{N_{\text{tw}}} \dot{\gamma}^{\beta} (\mathbf{s}^{\beta} \otimes \mathbf{m}^{\beta})}_{\text{twin in parent}}$$

$$(4)$$

where  $N_s$  and  $N_{\rm tw}$  respectively refer to the numbers of slip and twin systems in the parent region with current slip/twin plane normal and direction vectors denoted by  $\mathbf{m}^i$  and  $\mathbf{s}^i$ , respectively and  $i = \alpha$  or  $\beta$ . In Eq. (4),  $\dot{\gamma}^i$  is the shear rate on the ith system and  $\phi^\beta$  is the twin volume fraction of the  $\beta$ th twin system. The model accounts for  $N_s = 18$  slip and  $N_{\rm tw} = 12$  twin systems, Table 1.

The slip rate on the ith slip system is constitutively given by:

$$\dot{\gamma}^{i} = \dot{\gamma}_{0} \left| \frac{\tau^{i}}{g^{i}} \right|^{1/m} \operatorname{sgn}(\tau^{i}) \qquad ; \qquad g^{i} = \tau_{0}^{i} + \int_{0}^{t} (\dot{g}_{sl}^{i} + \dot{g}_{tw-sl}^{i}) \, \mathrm{d}t$$
 (5)

where  $\tau^i = \sigma$ :  $(\mathbf{m}^i \otimes \mathbf{s}^i)$  is the resolved shear stress (RSS) based on Schmid's law,  $\dot{\gamma}_0$  is a reference slip rate, m is the rate-sensitivity exponent, and  $g^i$  is the current strength of the slip system, which accounts for the initial critical RSS,  $\tau^i_0$ , slip–slip  $(\dot{g}^i_{sl})$  and twin–slip

Table 1
Slip and twin systems in pure Mg considered in this work.

	Slip/twin plane	Slip/twin direction	Number of systems
Basal ⟨a⟩ slip	(0001)	⟨11 <del>2</del> 0⟩	3
Prismatic $\langle a \rangle$ slip	$\{10\bar{1}0\}$	⟨11 <del>2</del> 0⟩	3
Pyramidal $\langle a \rangle$ slip	{1011}	⟨11 <del>2</del> 0⟩	6
Pyramidal $\langle c + a \rangle$ slip	{1122}	⟨112̄3⟩	6
Extension twinning (ET)	{1012}	⟨1011⟩	6
Contraction twinning (CT)	{1011}	$\langle 10\bar{1}\bar{2}\rangle$	6

 $(\dot{g}^{i}_{tw-s})$  interactions. The hardening due to slip–slip interactions is given by:

$$\dot{g}_{\rm sl}^i = \sum_{i=1}^{N_s} h_{ij}(\bar{\gamma})\dot{\gamma}^j \tag{6}$$

where hardening moduli  $h_{ij}$  are taken to depend on the total accumulated shear strain  $\bar{\gamma}$ :

$$h_{ij} = \begin{cases} h(\bar{\gamma}) & (i = j, \text{ self hardening}) \\ qh(\bar{\gamma}) & (i \neq j, \text{ latent hardening}) \end{cases} ; \qquad \bar{\gamma} = \sum_{i=1}^{N_s} \int_0^t |\dot{\gamma}^i| dt$$
 (7)

with q the latent hardening coefficient. Motivated by experimental observations on Mg single crystals, we adopt a linear hardening model for the basal slip and a saturation type hardening for the non-basal slip:

$$h(\bar{\gamma}) = \begin{cases} h_0, & \text{(basal slip)} \\ h_0^i \operatorname{sech}^2 \left| \frac{h_0^i \bar{\gamma}}{\tau_s^i - \tau_0^i} \right|, & \text{(non - basal slip)} \end{cases}$$
 (8)

where  $h_0^i$  is the initial hardening modulus and  $\tau_s^i$  is the saturation stress of the *i*th slip system. The effect of twinning (cf. Table 1) on slip hardening is given by:

$$\dot{g}_{\text{tw-sl}}^{\beta} = \begin{cases}
h_{\text{et_sl}}^{\beta} \text{sech}^2 \left| \frac{h_{\text{et_sl}}^{\beta} \bar{\gamma}_{\text{et}}}{\tau_{\text{set}}^{\beta} - \tau_{0,\text{et}}^{\beta}} \right| \dot{\gamma}^{\beta}, & \text{(ET)} \\
\frac{1}{2} (H_{\text{ct_sl}} / \sqrt{\bar{\gamma}_{\text{ct}}}) \dot{\gamma}_{\text{ct}}, & \text{(CT)}
\end{cases}$$

The rate of twinning on the  $\beta^{th}$  system is determined by:

$$\dot{\gamma}^{\beta} = \dot{\phi}^{\beta} \gamma^{\text{tw}} \qquad ; \qquad \dot{\phi}^{\beta} = \dot{\phi}_0^{\beta} \left( \frac{\tau^{\beta}}{s^{\beta}} \right)^{1/m_t} \tag{10}$$

where  $\gamma^{\text{tw}}$  is the theoretical twinning shear,  $\tau^{\beta}$  is the RSS, as above, and  $s^{\beta}$  is the current strength of the  $\beta^{\text{th}}$  twin system, given by:

$$s^{\beta} = \tau_0^{\beta} + \int_0^{t_i} (\dot{s}_{tw}^{\beta} + \dot{s}_{sl-tw}^{\beta}) dt \tag{11}$$

The contribution of twin-twin interactions is specified through The contribution of twin-twin interactions is given by:

$$\dot{s}_{tw}^{\beta} = \begin{cases}
h_{et}^{\beta} \operatorname{sech}^{2} \left| \frac{h_{et}^{\beta} \dot{\tau}_{et}}{\tau_{s}^{\beta} - \tau_{0}^{\beta}} \right| \dot{\gamma}^{\beta} & (ET) \\
H_{ct} \left( \sum_{m=1}^{N_{ct}} f_{m} \right)^{b} \dot{\gamma}^{\beta} & (CT)
\end{cases}$$
(12)

where  $h_{\rm et}^{\beta}$  and  $\tau_{\rm s\_et}^{\beta}$  are respectively the initial hardening modulus and the saturation stress for ET, and  $\bar{\gamma}_{\rm et}$  is the total shear strain on all ET systems. In Eq. (12)<sub>2</sub>,  $N_{\rm ct}$  is the total number of CT systems, and  $H_{\rm ct}$  and b are hardening parameters. Following Zhang and Joshi (2012),  $\dot{s}_{\rm sl-tw}^{i}$  is taken to be zero for both twin modes.

Twinning-induced lattice reorientation is taken to occur when the accumulated twin volume fraction,  $\bar{\phi} = \sum_{i}^{N_{\rm tw}} \phi_i$ , reaches a critical value  $\phi_{cr} = 0.9$  based on the comparison between single crystal simulations and experiments (Zhang and Joshi, 2012; Kelley and Hosford, 1967). The twin system that possesses the largest twin volume fraction is chosen as the orientation of the twinned lattice.

#### 3. Results

In all calculations, the initial porosity  $f_0=0.01$  and the initial cell aspect ratio  $\lambda_0=1$  are kept fixed. The initial void aspect ratio is varied in the range  $1/30 \le W_0 \le 1$ . This amounts to varying the initial ligament parameter  $0.27 \le \chi_0 \le 0.83$ ; see Fig. 1.

Table 2
Material parameters chosen for pure Mg.

	$\tau_0$ (MPa)	$h_0$ (MPa)	$\tau_s$ (MPa)	
Basal slip Prismatic $\langle a \rangle$ slip Pyramidal $\langle a \rangle$ slip Pyramidal $\langle c + a \rangle$ slip	0.5 25 25 40	20 1500 1500 3000	-	
			85 85 150	
	$\tau_0$ (MPa)	h <sub>et</sub> (MPa)	$\tau_{s_{}et}$ (MPa)	$h_{\rm et\_sl}$ (MPa)
Extension twinning	3.5	100	20	100
	$\tau_0$ (MPa)	H <sub>ct</sub> (MPa)	H <sub>ct_sl</sub> (MPa)	b
Contraction twinning	55	6000	15	0.05

Table 3
Crystal orientations considered in the cell model. Global orientations are shown in parenthesis.

Case	Loading direction (y)	Lateral direction $(x)$	Lateral direction $(z)$
Prismatic	[1210]	[1010]	[0001]
⟨c⟩-axis	[0001]	[1210]	[10Ī0]

Here, material parameters representative of pure Mg are used; see Table 2. Also,  $\dot{\gamma}_0 = 0.001 \text{ s}^{-1}$ ,  $m = m_t = 0.02$ , q = 1,  $\gamma^{\text{tw}} = 0.129$  and 0.138 for ET and CT, respectively, and  $\dot{\phi}_0^\beta = 0.001 \text{ s}^{-1}$  for all ET systems and  $\dot{\phi}_0^\beta = 0.0001 \text{ s}^{-1}$  for all CT systems. In addition, transverse isotropy is assumed for the elastic stiffness, which is characterized by five independent constants,  $C_{11} = 59.40$ ,  $C_{12} = 25.61$ ,  $C_{13} = 21.40$ ,  $C_{33} = 61.60$  and  $C_{44} = 16.40$  (all in GPa).

Two crystal orientations are considered, Table 3, as in Selvarajou et al. (2019). In the prismatic orientation, slip is expected to be the primary deformation mechanism, and large anisotropy is expected in the transverse ([1 $\bar{2}$ 10] – [0001]) plane. In the  $\langle c \rangle$ -axis orientation, extension twinning is favored. All calculations are pursued until well after the onset of void coalescence, i.e. when the cell's mode of deformation shifts to uniaxial stretching (Koplik and Needleman, 1988). The strain at the onset of coalescence ( $E_{eq}^c$ ) is simply detected by the saturation of the overall lateral strains ( $E_{xx}$  and  $E_{zz}$ ). In some cases, such transition does not occur and nominal failure is defined when  $\chi$  reaches 0.925.

#### 3.1. Prismatic loading

#### 3.1.1. Overall response

First, consider the case of uniaxial tension ( $\mathcal{T}=1/3$ ). Fig. 2 shows macroscopic responses along with the corresponding evolution of key parameters for various values of the initial void aspect ratio. The response of the pristine (void-free) matrix is also shown for reference. It is dominated by prismatic slip with early saturation hardening. Considering the porosity level (starting from  $f_0=0.01$ ), the response of the cell is always weaker than the matrix. The flatter the void the weaker the cell. However, even for this simple case of (remote) uniaxial tension, subsequent hardening of the cell depends on microstructure evolution.

For a moderately oblate void ( $W_0 = 1/2$ ), the response is similar to the  $W_0 = 1$  case (spherical void), Fig. 2(a). It is characterized by small-strain hardening, followed by limited softening, saturation and re-hardening at large strains. In both cases, there is modest porosity growth at the beginning (Fig. 2(b)) which explains the small-strain softening. Subsequently, the porosity saturates since all void elongation (Fig. 2(c)) is compensated for by lateral void shrinking (i.e. decrease in  $\chi_x$ ; see Fig. 2(d)). By way of consequence, failure does not occur in these cases. For the sake of clarity, the  $W_0 = 1$  case is not shown in Fig. 2(d).

With further increasing void oblateness (i.e. with decreasing the value of  $W_0$ ) void growth becomes significant, Fig. 2(b). For the  $W_0 = 1/30$  and  $W_0 = 1/20$  cases, the porosity-induced weakening eventually leads to early failure, which is marked by 'x' in Fig. 2(d). Failure here means attainment of the criterion  $\chi = 0.925$ , Fig. 2(d).

For intermediate values of  $W_0$ , early failure is prevented. Interestingly, the  $W_0 = 1/10$  stress–strain curve tends toward that of the pristine matrix until failure eventually occurs, but the  $W_0 = 1/6$  stress–strain curve crosses that of the matrix at  $E_{\rm eq} \sim 0.4$  and goes above it. It is remarkable that the porous cell hardens when the constituent matrix does not; see Section 3.1.2.

The results in Fig. 2 show evidence for induced anisotropy. This comes in part from void elongation, as predicted in cell calculations that employ  $J_2$  flow theory (Lassance et al., 2006). There is also deviation from axially symmetric shapes, induced by plastic anisotropy in transverse planes (i.e. normal to the applied stress). This behavior manifests when probing either the void aspect ratio (Fig. 2(c)) or the ligament parameter (Fig. 2(d)). For convenience, W is normalized by its initial value. The flatter the void the weaker the in-plane void anisotropy (i.e.  $W_x \sim W_z$ ). However, the cell anisotropy develops stronger in such cases (i.e.  $\chi_x \neq \chi_z$ ). This will be elucidated further in Section 3.1.2.

Next, consider the case of triaxial loading with  $\mathcal{T}=3$ , Fig. 3. For reference, the response of the pristine matrix is also plotted in Fig. 3. The lateral stresses now favor some activation of extension twinning, which is exacerbated in the voided cell. The effect of void shape on the effective response is quite strong, Fig. 3(a). The  $W_0=1/30$  cell is so much weaker than the pristine matrix and this is attributed to (i) twinning-induced softening, and (ii) porosity-induced softening, Fig. 3(b). Both aspects are void-mediated, since twinning itself is induced by the void. The signature of twinning manifests in the sigmoidal stress–strain responses.

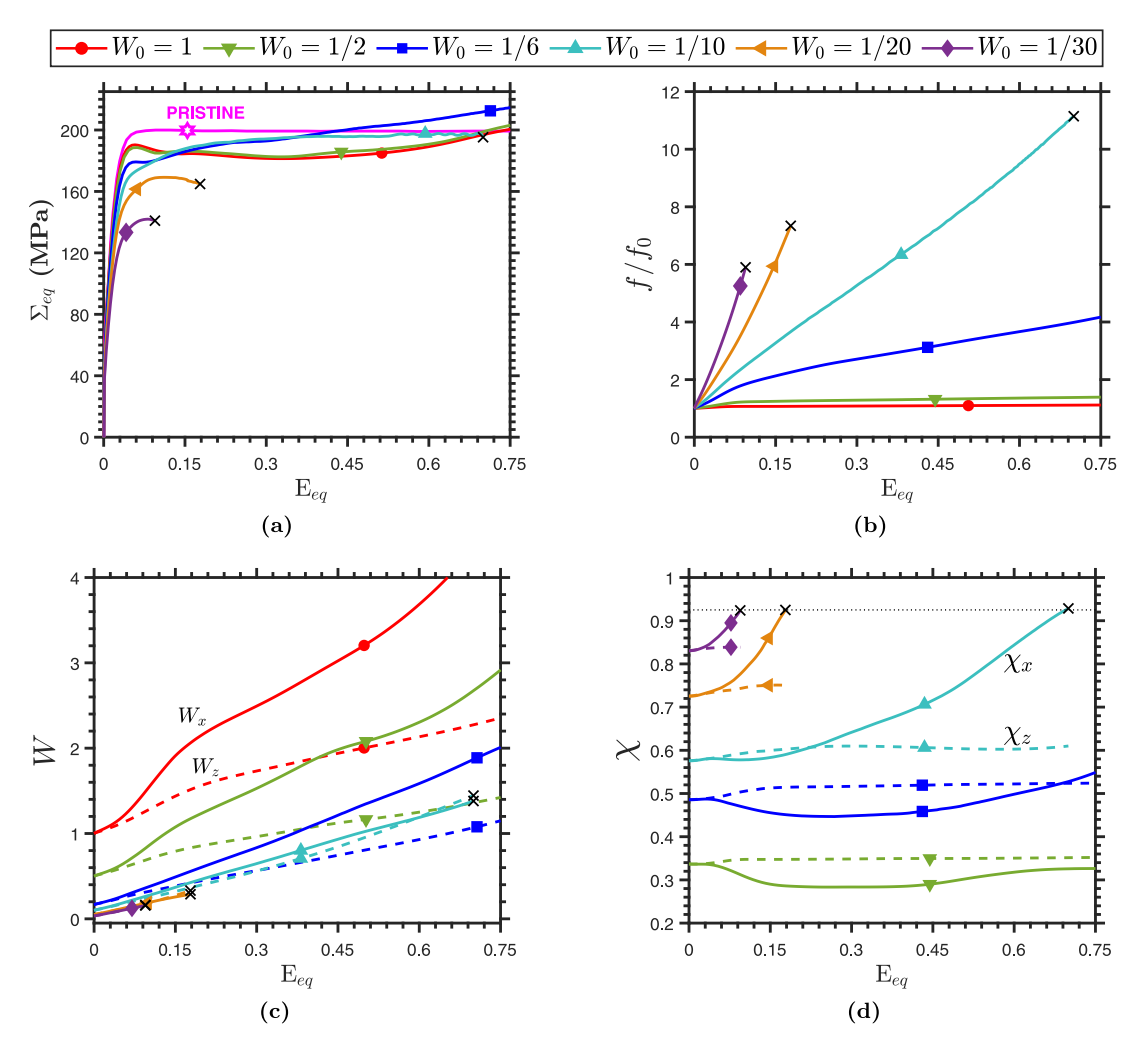


Fig. 2. Prismatic loading at T = 1/3: Equivalent strain  $E_{\text{eq}}$  versus: (a) equivalent stress,  $\Sigma_{\text{eq}}$ , (b) normalized porosity,  $f/f_0$ , (c) void aspect ratio, W, and (d) ligament parameter,  $\chi$ , for various values of  $W_0$ . Both, W and  $\chi$  are directional quantities; see text.

Here, failure occurs by the onset of void coalescence. Remarkably, the evolution of porosity does not depend much on  $W_0$ , Fig. 3(b). This is consistent with results obtained for a  $J_2$  matrix (Lassance et al., 2006). At high triaxiality, the dilational part of the cell's deformation is set by the hydrostatic component of the applied stress. Yet, the strain to failure ( $E_{eq}^c$ ) varies with  $W_0$ . The minimum strain to failure is below 0.04 for  $W_0 = 1/10$  and the maximum is about 0.08 for  $W_0 = 1$ . This implies that a failure criterion that is based on attaining a critical porosity ( $f = f_c$  independent of  $W_0$ ) would be insufficient.

The in-plane void- and cell-shape changes that were noted under uniaxial loading are negligible for  $\mathcal{T}=3$  until void coalescence sets in; see Figs. 3(c) and 3(d). Also, after the onset of coalescence, W decreases for  $W_0=1$  (much like in a  $J_2$  matrix). In contrast, initially oblate voids continue to open up along the primary loading direction even after the coalescence onset.

Additional results obtained for  $\mathcal{T} = 1$  do not exhibit a transition to sigmoidal stress–strain response, although the evolution of W,  $\chi$ , and f is qualitatively similar to  $\mathcal{T} = 3$ . The reader is referred to Indurkar (2020) for details.

# 3.1.2. Deformation micromechanics

To each deformation (slip or twin) mechanism, a relative activity  $\zeta^i$  is associated, defined as

$$\zeta^{i} = \frac{\dot{\gamma}^{i}}{\sum_{j=1}^{N_{s}+N_{\text{tw}}} \dot{\gamma}^{j}} \tag{13}$$

where  $\dot{\gamma}^i$  denotes the shear rate of the ith mechanism; see Eq. (4). Fig. 4 shows key mechanism activity distributions in the  $W_0=1/2$  and  $W_0=1/20$  cells deformed at  $\mathcal{T}=1/3$ . Contours show the central yz-plane at increasing overall strain  $E_{\rm eq}$ . Each contour consists of four quadrants stitched together:  $\zeta^{\rm bas}$ . (top-left quadrant),  $\zeta^{\rm ET}$  (top-right),  $\zeta^{\rm pris}$ . (bottom-right), and  $\zeta^{\rm pyr}$ . (bottom-left).

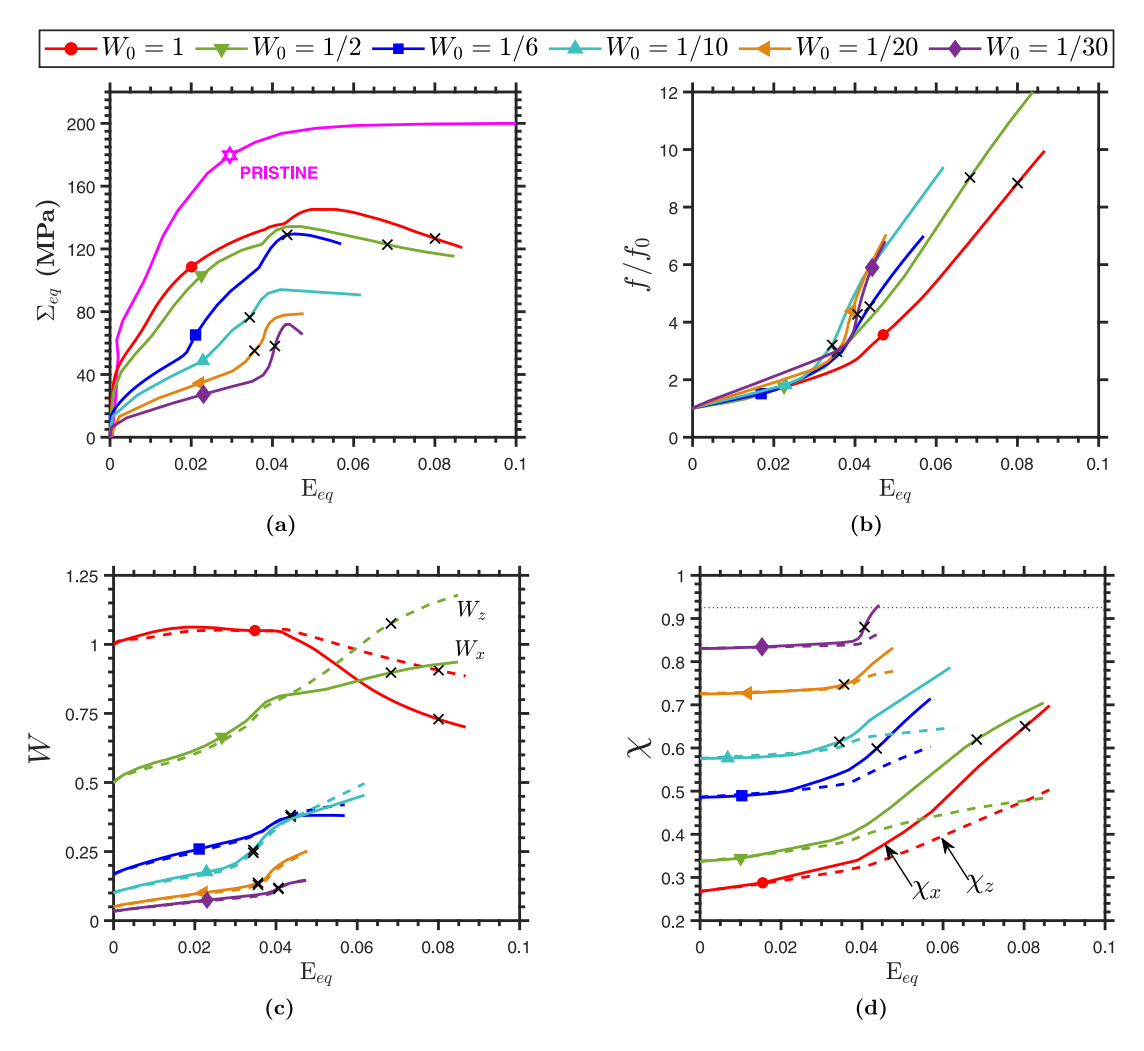


Fig. 3. Prismatic loading at T = 3: Equivalent strain  $E_{eq}$  versus: (a) equivalent stress,  $\Sigma_{eq}$ , (b) normalized porosity,  $f/f_0$ , (c) void aspect ratio, W, and (d) ligament parameter,  $\chi$ , for various  $W_0$  values.

For  $W_0 = 1/2$  (Figs. 4(a)–4(c)),  $\zeta^{\text{pris.}}$  is the primary mechanism, as would be expected in a matrix without a void. At early stages of deformation, basal and pyramidal  $\langle c + a \rangle$  slip proceed from concentrations at the void's equator while ET is prominent at the poles. With increasing strain, the ET regions reorient and thereafter accrue  $\zeta^{\text{bas.}}$  and  $\zeta^{\text{pyr.}(c+a)}$ .

For  $W_0 = 1/20$  (Figs. 4(d)-4(f)), ET activity occupies a much larger region of the matrix from the pole upward. This effectively screens prismatic slip, causing a drop in its contribution to the overall plasticity. Twinning induced reorientation paves way for pyramidal  $\langle c + a \rangle$  slip and, to a lesser extent, basal slip.

Transverse anisotropy can be evidenced by comparing longitudinal yz and xy sections. For small oblateness, e.g.  $W_0 = 1/6$ , the x-and z-dimensions of the void are quite different (Fig. 2(c)) but the cell's dimensions are nearly equal (Fig. 2(d)). For large oblateness, the opposite trend is observed. To illustrate salient differences consider the  $W_0 = 1/20$  case, Fig. 5. The pervasive nature of ET is immediately clear. However, plasticity in the x-ligament is governed by prismatic slip whereas that of the z-ligament carries mostly pyramidal  $\langle c + a \rangle$  slip. The highly anisotropic nature of these two plastically hard mechanisms translates to anisotropic thinning of the two ligaments, as shown in Fig. 2(d); compare the evolution of  $\chi_x$  and  $\chi_z$ .

The preceding observations highlight the critical role of void oblateness in damage evolution and anisotropic deformation under uniaxial tension. Next, Fig. 6 shows the effect of triaxiality on the activation of various mechanisms around the void for fixed  $W_0$  (here equal to 1/6). In effect, there is a transition from a prismatic mode of deformation to a twinning mode with increasing triaxiality, and this reflects in the stress–strain behavior as well. The increasingly important role of ET with increasing  $\mathcal{T}$  is clear by inspecting Figs. 6(a), 6(d), and 6(g). Twinning under uniaxial tension is solely the effect of  $W_0$  as no applied lateral tensile stresses exist whereas at higher  $\mathcal{T}$  the void-shape effect on twinning is enhanced by the applied lateral stresses. As a result, at  $\mathcal{T} = 1/3$  prismatic slip dictates yield, because twinning plasticity is largely constrained within the volume deforming by prismatic slip. Later, twinning-induced reorientation enhances strain hardening by activating pyramidal  $\langle c + a \rangle$  slip; see Fig. 2(a). On the other hand,

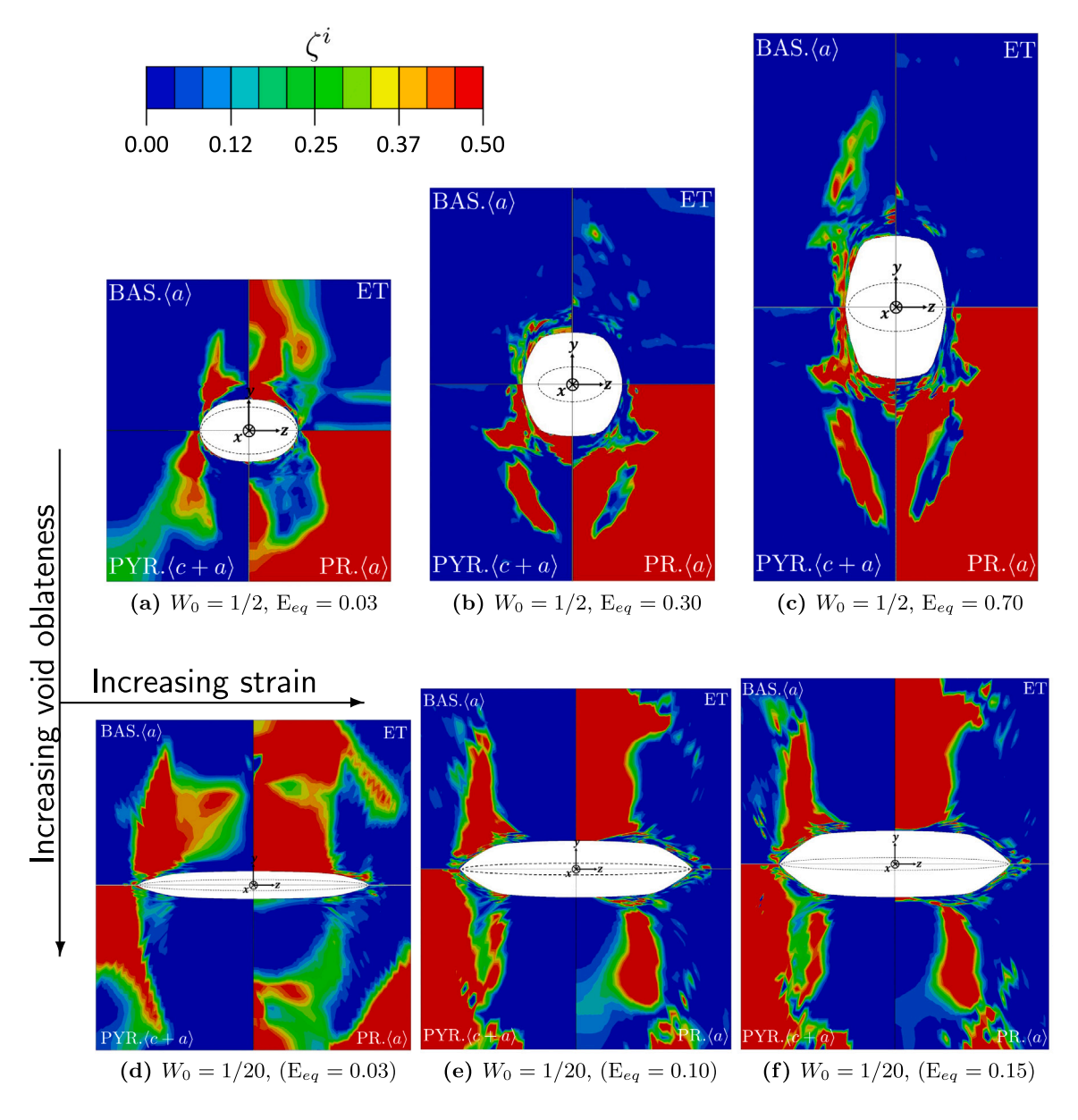


Fig. 4. Prismatic loading at T = 1/3: Evolution of deformation mechanism activity (Eq.  $(14)_1$ ) with strain on the mid-yz plane of the unit cell for (a)-(c)  $W_0 = 1/2$  and (d)-(f)  $W_0 = 1/20$ .

at  $\mathcal{T}=3$ , the soft ET mode is profuse enough to induce a much lower yield stress. Subsequent reorientation brings about the high strain hardening effect seen in Fig. 3(a).

The volume-averaged relative activity of the *i*th deformation mechanism,  $\bar{\xi}^i$ , and average twinning volume fraction,  $\bar{\phi}^i$ , are calculated using:

$$\bar{\zeta}^{i} = \frac{\int \dot{\gamma}^{i} dV}{\int \sum_{i=1}^{N_{s}+N_{tw}} \dot{\gamma}^{j} dV}, \quad \bar{\phi}^{i} = \frac{1}{V} \int \phi^{i} dV$$
(14)

with  $\dot{\gamma}^i$  as above.

The relative activities under uniaxial loading are shown in Figs. 7(a) and 7(b). The results are displayed for various values of  $W_0$  and correspond to the stress–strain curves in Fig. 2(a). The plastic flow in the pristine material is uniform and entirely dominated

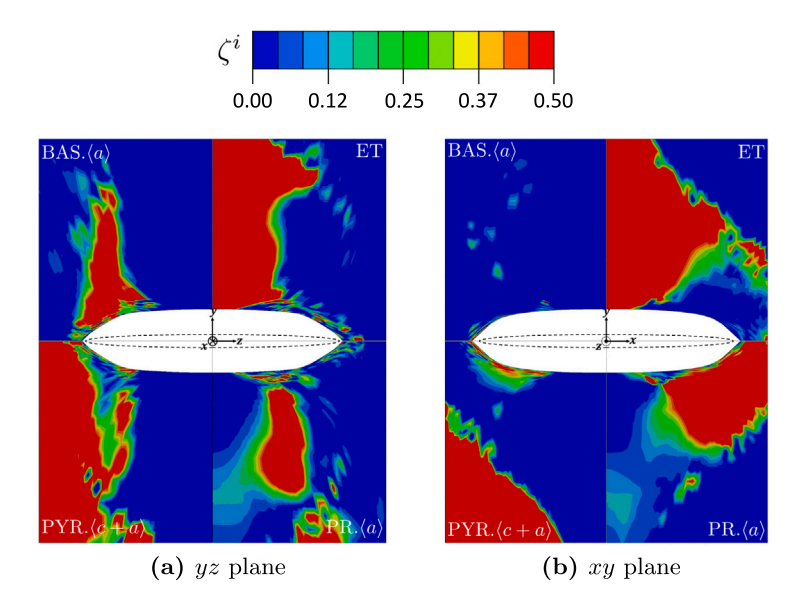


Fig. 5. Prismatic loading at T = 1/3: Anisotropy of deformation mechanism activity around a penny-shaped void  $(W_0 = 1/20)$  at  $E_{eq} = 0.10$ .

by prismatic  $\langle a \rangle$  slip; all other  $\bar{\zeta}^i$  are zero. As shown in the top plot of Fig. 7(a), the contribution of prismatic slip decreases with increasing void oblateness. This gives rise to an increasing contribution of pyramidal  $\langle c + a \rangle$  slip (bottom of Fig. 7(a)) as well as the plastically soft basal slip and extension twinning (Fig. 7(b)).

At  $\mathcal{T}=3$ , there is a transition in the primary deformation mechanism imparted by twinning induced crystal reorientation, Figs. 7(c) and 7(d). Before reorientation, which occurs between  $E_{\rm eq}\sim0.03$  and  $E_{\rm eq}\sim0.04$ , the trends are similar to the case of uniaxial loading, except that ET is much more dominant at high triaxiality (top of Fig. 7(d)). This is simply due to the contribution of a strong lateral stress  $\Sigma_{zz}$  oriented along the  $\langle c \rangle$  axis; see Table 3. The dominance of ET increases with void oblateness. After reorientation, however, pyramidal  $\langle c+a \rangle$  slip becomes the primary deformation mechanism (bottom of Fig. 7(c)). Throughout, basal slip remains an important secondary mechanism (bottom of Fig. 7(d)). This complex interplay of evolving anisotropy and void shape effects lead to the stress–strain curves of Fig. 3(a).

Figs. 7(e)–7(g) summarize the effect of  $W_0$  on peak relative activity for various slip modes. Increasing oblateness leads to a monotonic decrease in prismatic  $\langle a \rangle$  slip, a trend that is exacerbated by triaxiality. On the other hand, pyramidal  $\langle c + a \rangle$  and basal slip contributions exhibit more complex coupling. For a given  $W_0$ , the contribution of these mechanisms generally increases with increasing  $\mathcal{T}$ . However, for a given  $\mathcal{T}$ , while the contribution increases with increasing oblateness under uniaxial stress state (save for the prismatic  $\langle a \rangle$  slip), it is relatively insensitive to  $W_0$  at  $\mathcal{T}=1$  and  $\mathcal{T}=3$ .

Fig. 7(h) reveals the synergistic effect of stress triaxiality and initial oblateness on the ET volume fraction. For a given  $W_0$ , the increase in  $\bar{\phi}^{\rm ET}$  with increasing  $\mathcal T$  is expected. It is a result of the increased lateral tensile stress along the z-ligament, which promotes  $\langle c \rangle$ -axis extension. Furthermore, oblateness exacerbates this behavior at a fixed level of  $\mathcal T$ .

In summary of the prismatic loading case, the overall stress–strain responses in Figs. 2(a) and 3(a) are explained by the combined evolution of porosity and fine slip/twinning mechanisms. The effect of void shape on yield softening is a result of preferential activation of ET and basal slip in lieu of prismatic  $\langle a \rangle$  slip. The transition from saturation hardening to a sigmoidal response is a result of the compounding effect of stress triaxiality and initial oblateness on the twinned regions. For instance, in the  $W_0 = 1/20$  cell, nearly 50% of the matrix volume undergoes ET at  $\mathcal{T} = 1$ , and at  $\mathcal{T} = 3$  it is  $\sim 75\%$ . With continuing deformation, there is competition between porosity-induced softening and the material hardening induced by pyramidal  $\langle c + a \rangle$  slip that preferentially occurs in twinned regions. It turns out that for  $W_0 \gtrsim 1/10$  the material hardening prevails over ligament softening by virtue of the larger volume over which it occurs. For penny-shaped voids ( $W_0 \lesssim 1/10$ ), the rapid increase in the basal  $\langle a \rangle$  slip (accounting for  $\sim 25\%$  strain) induces more softening than less oblate voids ( $W_0 \gtrsim 1/16$ ).

## 3.2. $\langle c \rangle$ -axis loading

#### 3.2.1. Overall response

Consider the uniaxial tension case first, Fig. 8. Initial yield is governed by ET, followed by rapid hardening due to non-basal mechanisms resulting from twinning induced crystal reorientation until saturation, Fig. 8(a). For porous crystals with moderately oblate voids ( $W_0 \gtrsim 1/10$ ), the peak stress exceeds that of the pristine crystal. This arises due to the formation of twin sectors that activate non-basal slip, as in the  $W_0 = 1$  case, which is reproduced from Selvarajou et al. (2019). A detailed discussion on the non-basal slip activation due to the void induced twin sector formation is presented *et. seq.* (Sections 3.2.2 and 3.2.3).

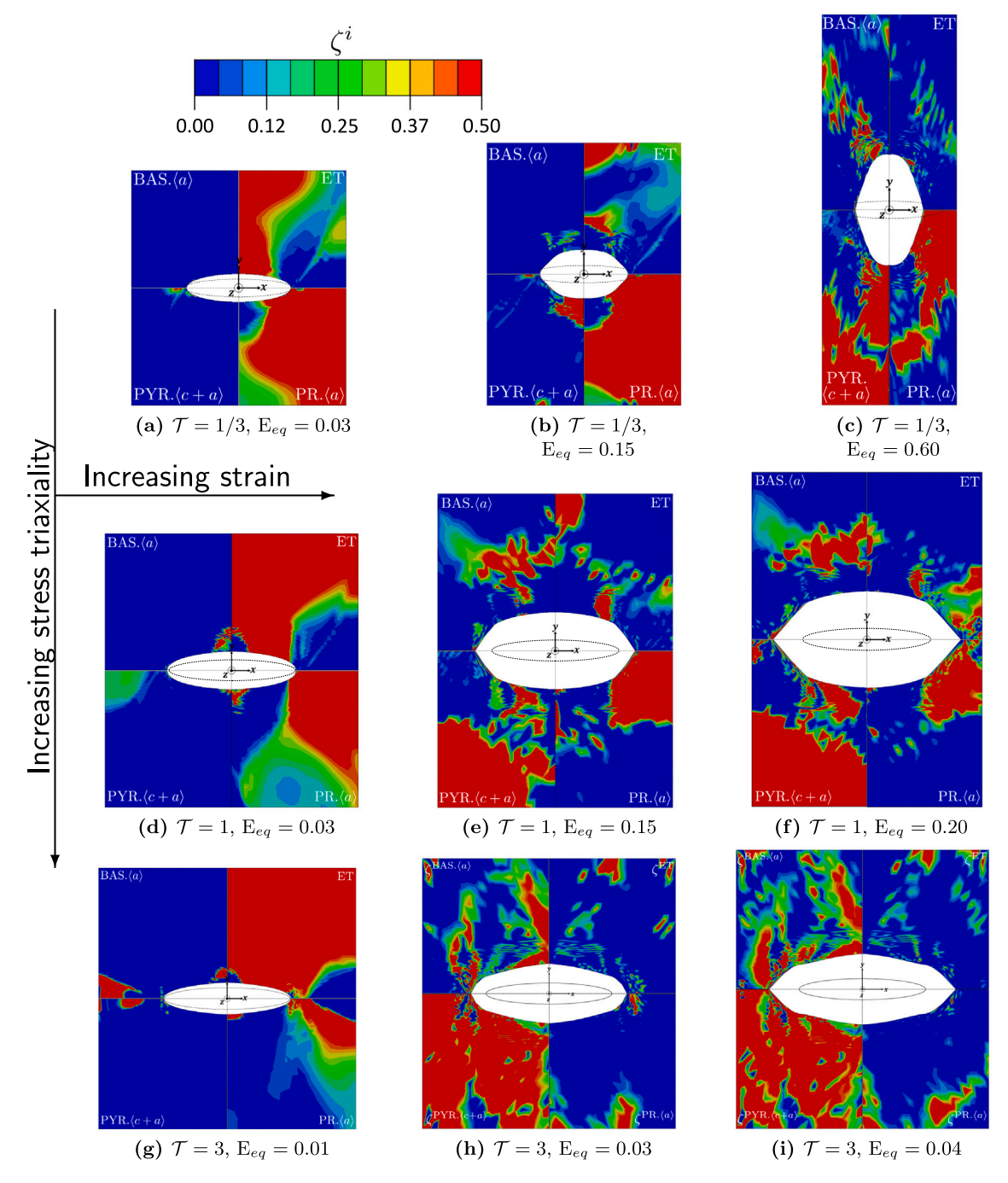


Fig. 6. Prismatic loading,  $W_0 = 1/6$ : Effect of stress triaxiality on the deformation mechanism activity ( $\zeta'$ , Eq. (14)<sub>1</sub>). The contours on the mid-xy plane are shown for illustration. Panels (a)–(c), (d)–(f) and (g)–(i) are respectively for  $\mathcal{T} = 1/3$ ,  $\mathcal{T} = 1$ , and  $\mathcal{T} = 3$ . Cells are shown as deformed.

For penny shaped voids ( $W_0 \lesssim 1/10$ ), the twinning induced increase in the peak stress is compensated for by void induced softening, Fig. 8(b). For nearly spherical voids ( $W_0 = 1$  or 1/2), the rate of porosity decrease is insensitive to  $W_0$ ; this explains their near identical stress–strain responses in Fig. 8(a). With increasing oblateness, porosity grows at faster rates. As in the prismatic loading case, the highly oblate voids ( $W_0 \lesssim 1/10$ ) exhibit enough growth leading to coalescence, unlike the moderately oblate voids ( $W_0 \lesssim 1/10$ ) for which the porosity tends to saturate.

The non-monotonic porosity growth for  $W_0 < 1/2$  is noteworthy. Growth is initially rapid, followed by a short stagnation regime, and ultimately transitions to a runaway growth. This behavior is also reflected in the void aspect ratio evolution, Fig. 8(c). Transverse anisotropy is here negligible ( $W_x \approx W_z$ ), in contrast with the case of prismatic loading (see Fig. 2(c)).

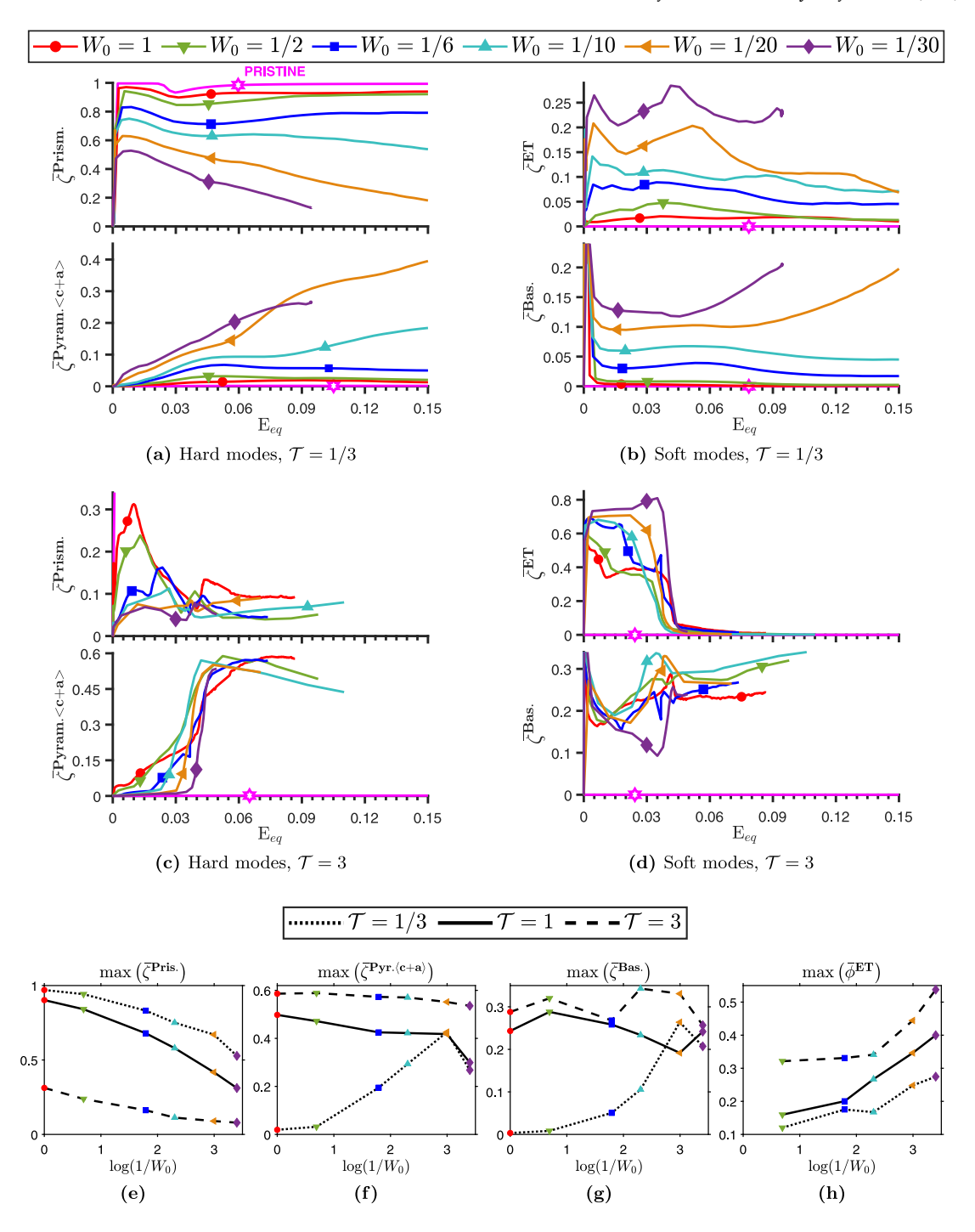


Fig. 7. Prismatic loading: Panels (a) and (c) show the evolution of average relative activity (Eq.  $(14)_1$ ) of the plastically softer modes  $(\bar{\xi}^{ET}, \bar{\xi}^{bas})$  for  $\mathcal{T} = 1/3$  and 3 respectively. Panels (b) and (d) show the plastically harder modes  $(\bar{\xi}^{pris}, \bar{\xi}^{pyr,(c+a)})$ . Panels (e)–(g) collate the peak relative activities of prismatic  $\langle a \rangle$ , pyramidal  $\langle c + a \rangle$  and basal  $\langle a \rangle$  slip respectively. Panel (h) shows maximum  $\bar{\phi}^{ET}$ .

For the intermediate triaxiality  $\mathcal{T}=1$ , void-induced hardening persists for sufficiently blunt voids ( $W_0\gtrsim 1/6$ ), Fig. 9(a). Fig. 9(b) shows the evolution of the ligament parameters (along transverse directions x and z) for all cases analyzed. Interestingly, no ligament thinning is observed in the twinning regime. All lateral growth occurs after twinning is complete. Here too, there is very little transverse anisotropy ( $\chi_x\approx\chi_z$  from Fig. 9(b) and  $W_x\approx W_z$  from Fig. 9(c)).

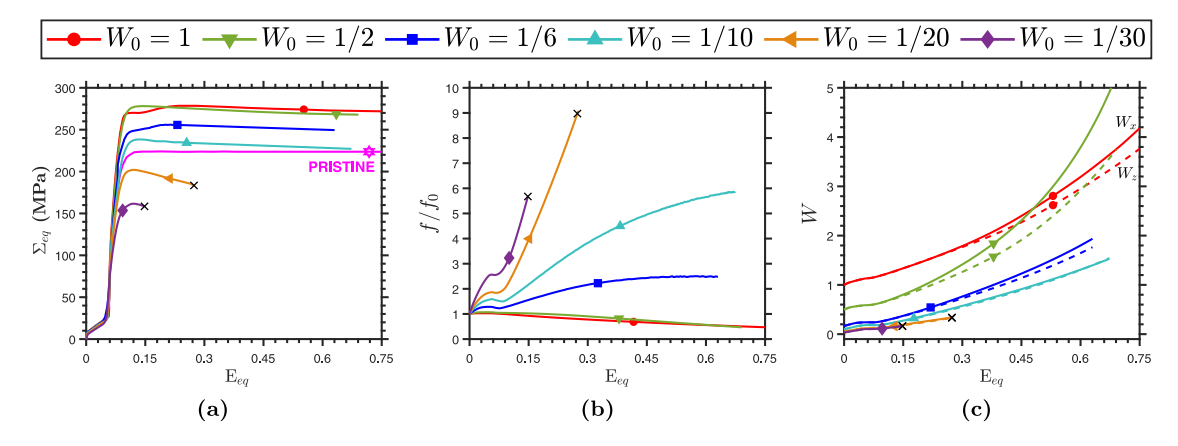


Fig. 8.  $\langle c \rangle$ -axis loading,  $\mathcal{T} = 1/3$ : Effect of initial void oblateness on (a) the stress-strain response, (b) porosity evolution, and (c) void aspect ratio.

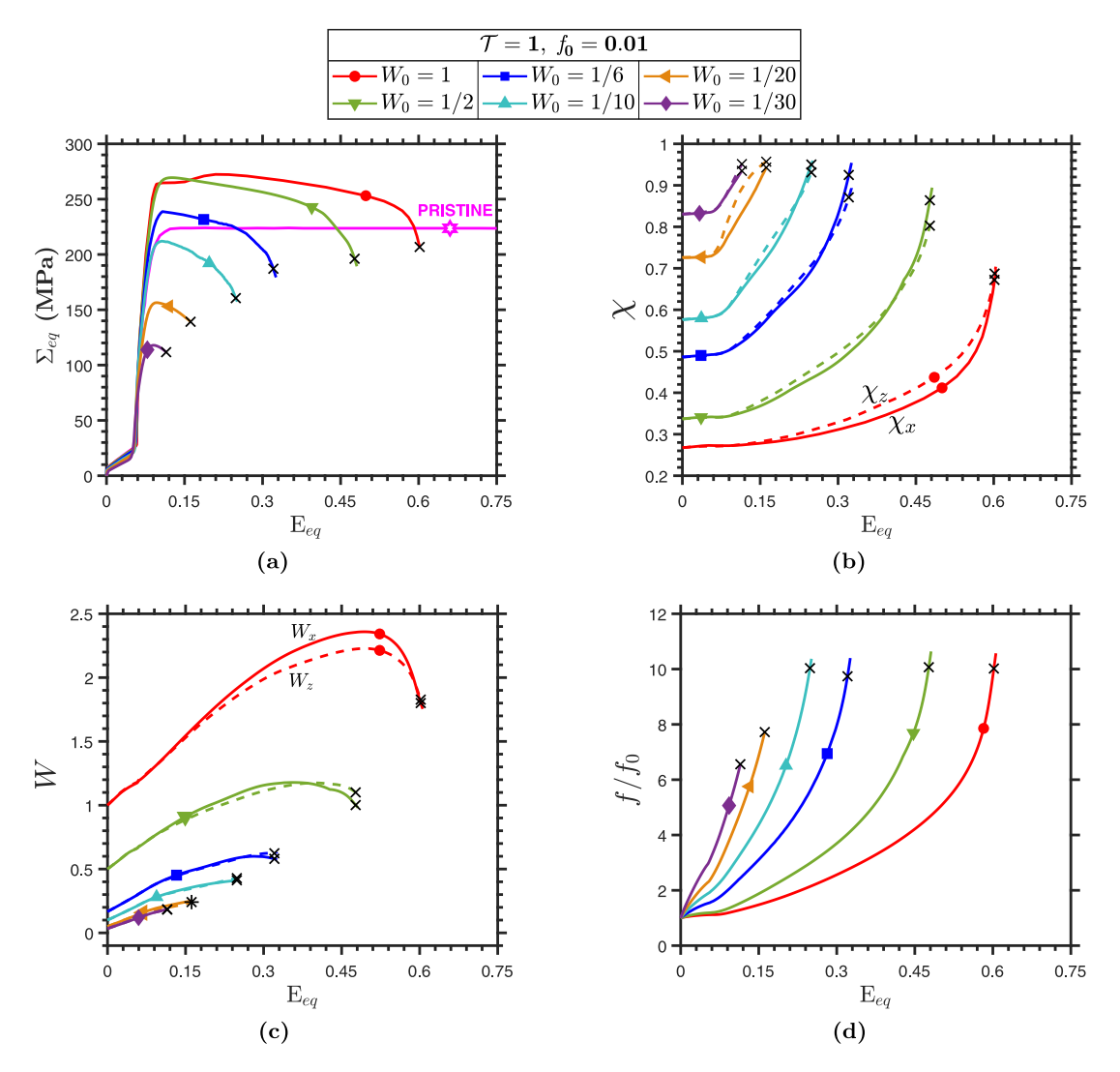


Fig. 9.  $\langle c \rangle$ -axis loading,  $\mathcal{T} = 1$ : Effect of initial void oblateness on (a) the stress–strain response, (b) ligament parameter, (c) void aspect ratio, and (d) porosity evolution.

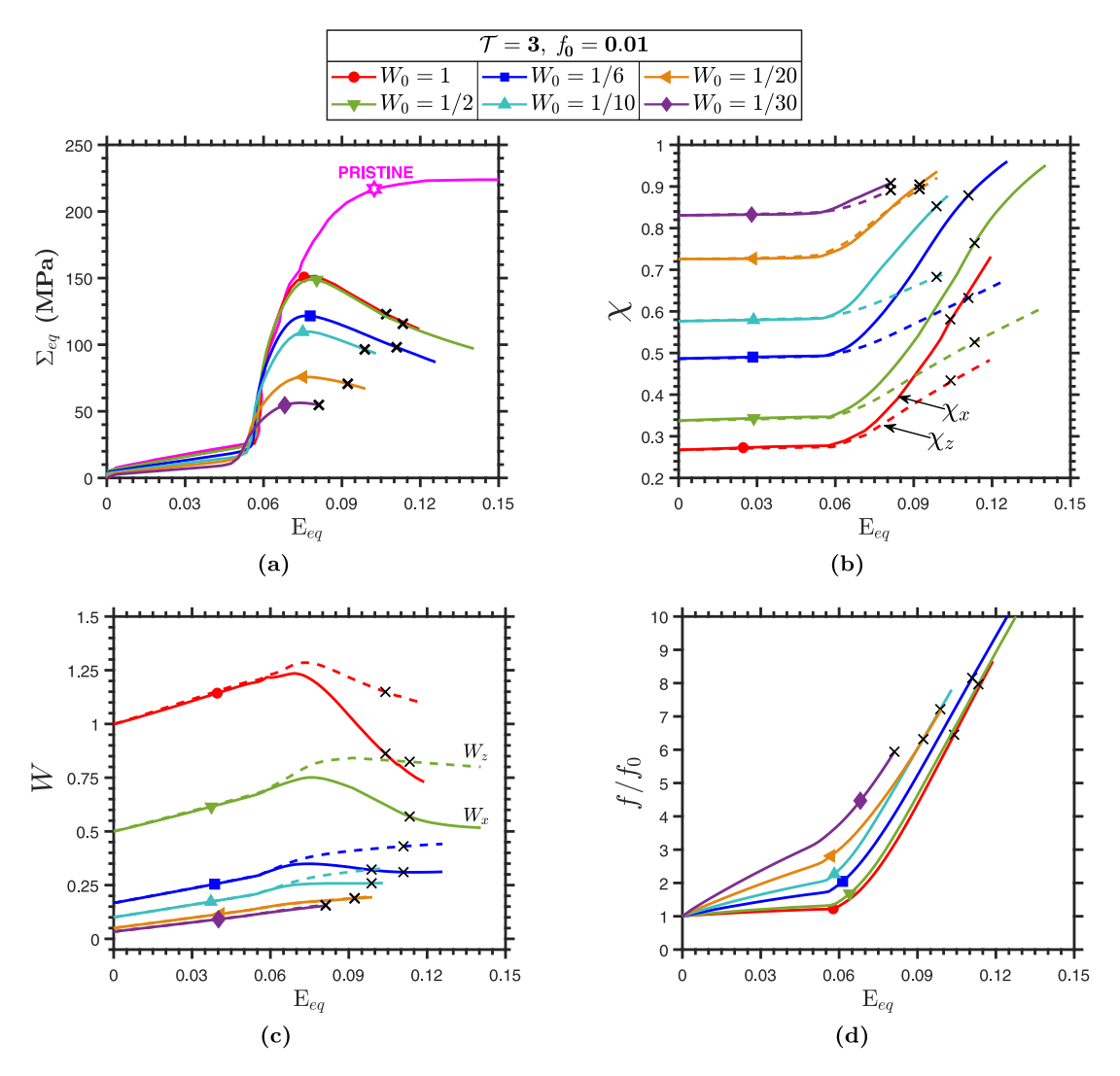


Fig. 10.  $\langle c \rangle$ -axis loading,  $\mathcal{T} = 3$ : Effect of initial void oblateness on (a) the stress–strain response, (b) ligament parameter, (c) void aspect ratio, and (d) porosity evolution.

The evolution of porosity is shown in Fig. 9(d). Twinning induced early porosity stagnation, which prevailed over the entire range of  $W_0$  for  $\mathcal{T} = 1/3$ , is seen here only for nearly spherical voids. The strain to failure,  $E_{eq}^c$ , decreases with increasing void oblateness.

Upon increasing the triaxiality to  $\mathcal{T}=3$ , some differences begin to emerge, Fig. 10. Notably, void-induced hardening is now absent (compare with Fig. 9). This is due to a faster rate of porosity growth at  $\mathcal{T}=3$ . The resulting softening prevails over void-induced hardening, which results from void-induced twinning. Just like in the  $\mathcal{T}=1$  case, ligament thinning is suppressed during twinning, Fig. 10(b). The effect is more visible here because the strain window is narrower. Remarkably, however, some anisotropy is eventually induced post-twinning. This manifests both in ligament thinning ( $\chi_x \neq \chi_z$ , Fig. 10(b)) and void shape evolution ( $W_x \neq W_z$ , Fig. 10(c)). Highly oblate voids ( $W_0 \lesssim 1/20$ ) appear to be an exception. Similar to  $\mathcal{T}=1$ , porosity stagnation during twinning is strong for near-spherical voids ( $W_0 \gtrsim 1/2$ ) but disappears with increasing oblateness, Fig. 10(d). In spite of such qualitative differences, the strain to failure is weakly sensitive to  $W_0$  at such high triaxiality.

# 3.2.2. Deformation micromechanics

Recall that under prismatic loading, increasing initial oblateness enhances extension twinning, which leads to a qualitative change in the stress–strain response especially at high levels of triaxiality. On the other hand, the stress strain response is largely of the sigmoidal type under  $\langle c \rangle$ -axis loading at similar triaxiality levels indicating that extension twinning remains the primary deformation mechanism

Consider the case of uniaxial tension. Figs. 11(a)-11(c) illustrate the type of deformation activity that develops for very oblate voids (here  $W_0 = 1/20$ ). The three stages are shown in Fig. 11(d). As noted earlier (see Fig. 8(b)), increasing initial oblateness renders

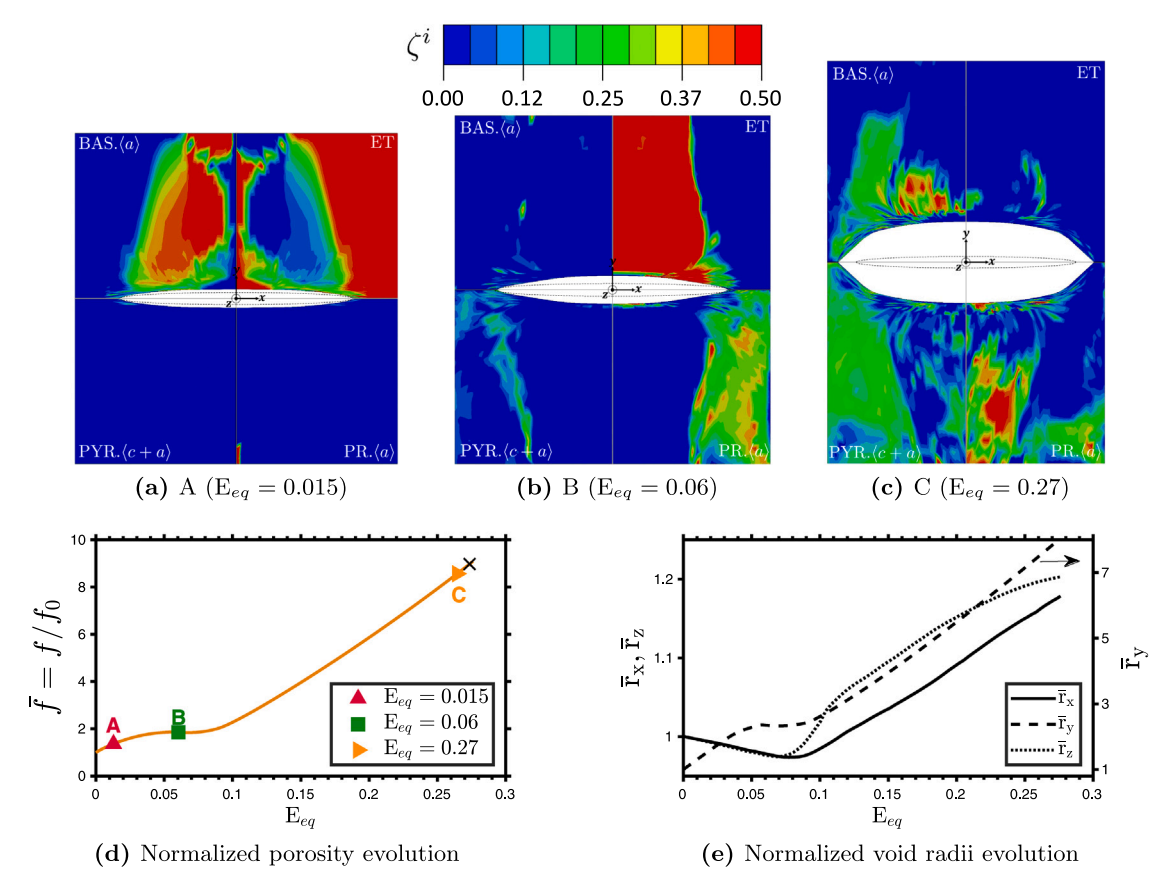


Fig. 11.  $\langle c \rangle$ -axis loading,  $\mathcal{T} = 1/3$ : Porosity evolution in a unit cell with  $W_0 = 1/20$ . Panels (a)—(c) show evolution of the relative activity distributions of key mechanisms in the xy-plane at three stages A, B and C. Panels (d) and (e) show the normalized porosity and void radii evolution.

the porosity evolution non-monotonic under  $\langle c \rangle$ -axis loading. At stage A, extension twinning is profuse in the lateral ligaments (Fig. 11(a)) while regions above and below the void pole are shielded from twinning and instead deform by basal slip. Upon straining to stage B, twinning-induced reorientation renders the ligament plastically harder due to prismatic  $\langle a \rangle$  slip (Fig. 11(b)). Thus, the matrix experiences a highly non-homogeneous strain hardening. The higher hardening at the equator results in temporary stagnation of porosity (point B, Fig. 11(d)). More specifically, the void cannot grow laterally, as illustrated in Fig. 11(e). The transverse void radii  $r_x$  and  $r_z$  decrease in the early stages. As twinning saturates in the ligament (0.05  $\lesssim E_{\rm eq} \lesssim 0.08$ ), the previously untwinned pole region now undergoes rapid twinning (Fig. 11(b)) and strain hardens. Once the entire matrix has twinned, the heterogeneity of hardening diminishes and the void undergoes a rapid evolution (B  $\rightarrow$  C) at an elevated stress level. Closer to coalescence (point C), the pyramidal  $\langle c + a \rangle$  and basal slip drive the final stages of the localization (internal necking) process.

For less oblate voids the distributions of relative activities are similar to this case, except that the polar region shielded from twinning is proportionally smaller with decreasing oblateness. As a result, the lateral void growth may be stagnant or slowly increasing, and this still reflects in the stagnation of porosity in the twinning-affected regime (Fig. 8(b)).

The shielding of the polar region from extension twinning and its subsequent unshielding reflects in the averaged relative activity maps shown in Fig. 12(a). Initially, the ET contribution to plastic deformation is smaller compared to the pristine response, but then gradually picks up as the polar region twins (cf. Figs. 11(a)–11(c)). This behavior is consistent for all  $W_0$  values. For highly oblate voids ( $W_0 \lesssim 1/10$ ) the ET activity prevails over the strain range that is more than twice the range for the spherical void. In this regime, both the  $\bar{\zeta}^{\text{pris.}}$  and  $\bar{\zeta}^{\text{pyr.}(c+a)}$  are also active (Fig. 12(b)). With increasing oblateness the prismatic slip contribution decreases and is replaced primarily by the pyramidal  $\langle c+a \rangle$ , and to some extent, basal slip.

The reason why the polar regions of the matrix do not twin despite a favorable loading orientation is that, in oblate voids  $\sigma_{yy}$  in the polar region is not sufficient to activate ET (Prasad et al., 2016). On the other hand, the local shear stresses  $\sigma_{xy}$  and  $\sigma_{yz}$  still exist, which aid basal slip.

Fig. 13 depicts an example of void shape effect in promoting basal slip in lieu of ET at a higher triaxiality level ( $\mathcal{T}=1$ ). With increasing oblateness, basal slip occupies increasingly larger matrix volume, roughly scaling with  $1/W_0^2$ . The matrix volume that is screened from ET is much less dependent on triaxiality but more so on the void shape, compare Fig. 11(a) with 13(b). Fig. 14 collates the peak relative activity levels of the dominant slip mechanisms (Fig. 14(a)-14(c)) and the maximum average ET volume fraction

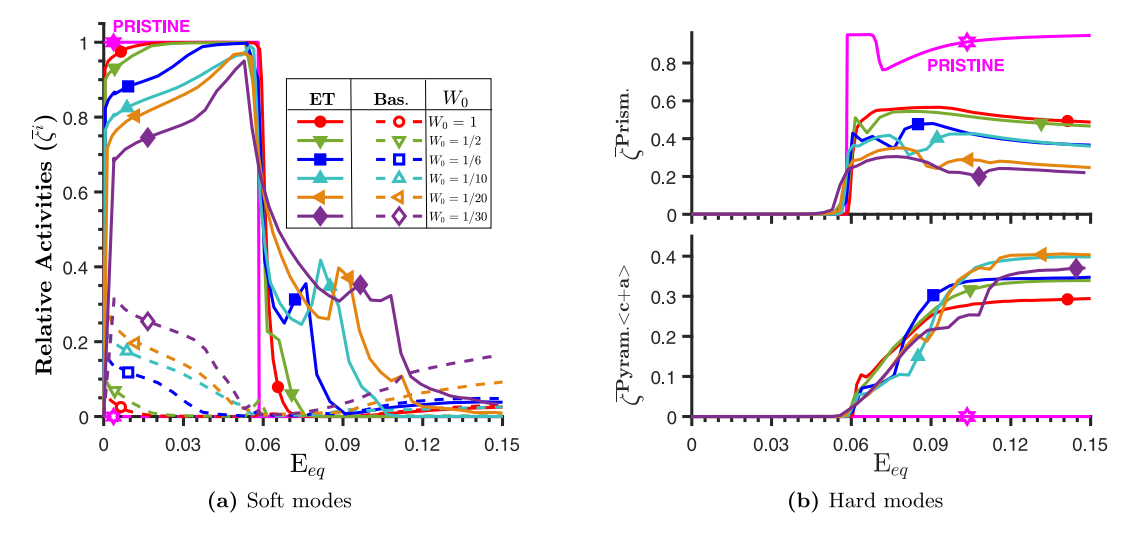


Fig. 12.  $\langle c \rangle$ -axis loading,  $\mathcal{T} = 1/3$ : Relative activity evolution of (a) plastically softer modes ( $\tilde{\zeta}^{\text{ET}}$ ,  $\tilde{\zeta}^{\text{bas}}$ ), and (b) plastically harder modes ( $\tilde{\zeta}^{\text{pris}}$ ,  $\tilde{\zeta}^{\text{pyr.}(c+a)}$ ).

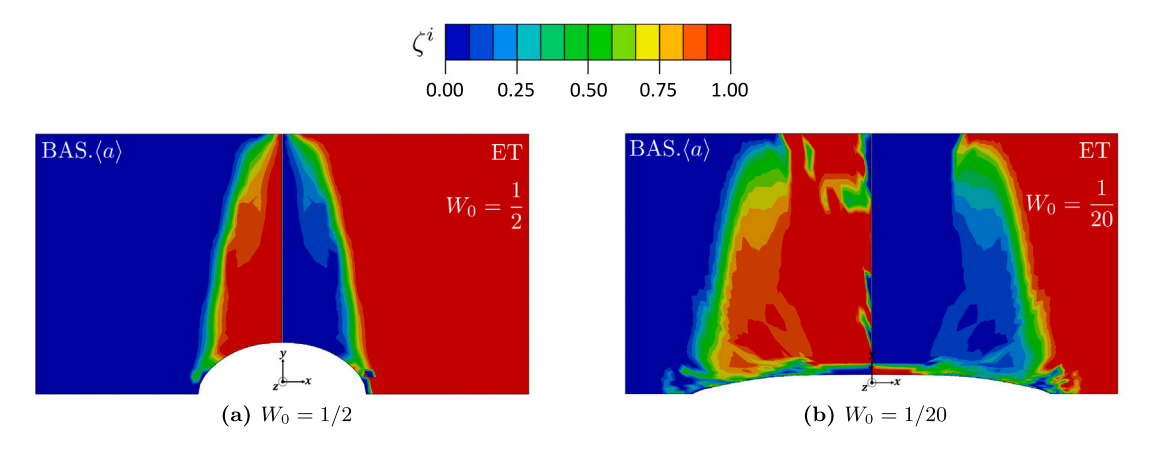


Fig. 13.  $\langle c \rangle$ -axis loading,  $\mathcal{T} = 1$ : Effect of void oblateness on the distribution of soft deformation mechanisms. The contours are shown at  $E_{eq} = 0.03$ , which reveal an increased activity of basal  $\langle a \rangle$  slip near the void pole with increasing void oblateness in lieu of extension twinning.

(Fig. 14(d)) as a function of  $W_0$  and  $\mathcal{T}$ . In contrast to the prismatic loading case where  $\bar{\phi}^{ET}$  increases with increasing oblateness and triaxiality, here the trend is the reversed. While extension twinning remains the preferred deformation mechanism, it is reduced by nearly 50% with increasing void oblateness (at a fixed  $\mathcal{T}$ ). For a given  $W_0$ , the decrease in  $\bar{\phi}^{ET}$  is about 10-15% with increasing  $\mathcal{T}$ .

The decrease in twinning activity is compensated by basal slip, whose contribution increases with increasing oblateness and triaxiality, Fig. 14(c). The post-twinning activity is governed by the prismatic and pyramidal  $\langle c + a \rangle$  slip mechanisms. While the prismatic slip activity decreases with increasing oblateness and triaxiality, the pyramidal  $\langle c + a \rangle$  slip contribution increases with increasing triaxiality (at a given  $W_0$ ) but decreases with increasing oblateness (at a fixed  $\mathcal{T}$ ). The evolution of these activities (not shown here) with deformation looks qualitatively similar to that of  $\mathcal{T} = 1/3$  (see Indurkar, 2020).

#### 3.2.3. Twin sector formation

Selvarajou et al. (2019) showed the formation of symmetry-breaking twin sectors in a porous HCP unit cell with a spherical void. Against that backdrop, Fig. 15 collates the effect of void shape in the formation of twin sectors. As seen, with increasing oblateness more twin variants are activated (for a given  $\mathcal{T}$ ), which are demarcated by twin sector boundaries with high misorientation ( $\sim 60^{\circ}$ ), shown as black dashed lines in Fig. 15. The twin sector formation is relatively insensitive to stress triaxiality but is more strongly governed by the void oblateness.

#### 3.3. Crystallographic aspects in void coalescence

Fig. 16 summarizes the results of the previous two sections in terms of the strain to failure,  $E_{eq}^c$ , versus a measure of void oblateness,  $\ln(1/W_0)$ . At all levels of triaxiality, ductility decreases monotonically with increasing oblateness.

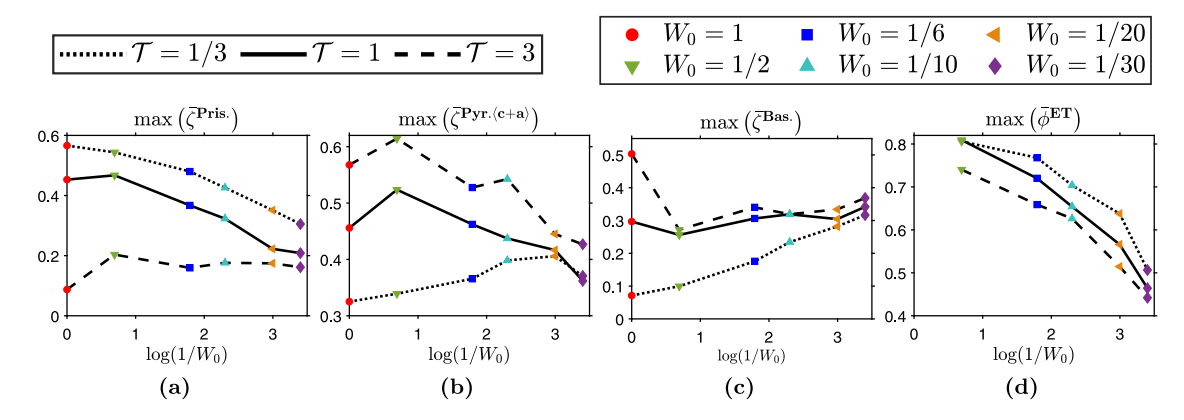


Fig. 14.  $\langle c \rangle$ -axis loading: Role of void shape and triaxiality in the peak values of (a) prismatic  $\langle a \rangle$  slip, (b) pyramidal  $\langle c + a \rangle$  slip, (c) basal slip activities, and (d) extension twin volume fraction.

At  $\mathcal{T}=1/3$  (Fig. 16(a)), coalescence only occurs for moderate to highly oblate voids, namely  $W_0\lesssim 1/10$  (prismatic case) and  $W_0\lesssim 1/20$  ( $\langle c \rangle$ -axis case). Moreover, for a given void aspect ratio  $W_0$ , the prismatic orientation is less ductile than the  $\langle c \rangle$ -axis orientation. As seen from Figs. 17(a) and 17(d), the void shape anisotropy in the xz-plane at failure ( $E_{eq}=E_{eq}^c$ ) is much stronger under prismatic loading. Moreover, there appear to be two different modes of coalescence in the prismatic case: ligament necking in the x-direction versus strain localization in the yz-plane. The localized deformation band in the yz-plane is a consequence of the localized basal slip, and tends to connect voids at 45° above and below the shown void. Note that, of the two lateral ligaments, the z-ligament is also more resistant to plastic deformation, which suggests that the emergence of the localized band is a consequence of the inability of the z-ligament to neck down, unlike the x-ligament. On the other hand, the  $\langle c \rangle$ -axis case shows a clear tendency to fail by inter-void ligament necking in the entire xz plane.

At  $\mathcal{T}=1$  (Fig. 16(b)), the prismatic orientation exhibits higher ductility for less oblate voids ( $W_0 \gtrsim 1/6$ ) compared to the  $\langle c \rangle$ -axis orientation. However, it decreases more rapidly with increasing oblateness ( $W_0 \lesssim 1/10$ ) relative to the  $\langle c \rangle$ -axis case. At  $\mathcal{T}=3$  (Fig. 16(c)),  $E_{eq}^c$  shows different trends. The prismatic orientation is consistently less ductile than the  $\langle c \rangle$ -axis orientation. For the  $\langle c \rangle$ -axis loading, the ductility dependence on the initial oblateness is relatively weak for  $W_0 \gtrsim 1/6$  but decreases rapidly for more oblate voids. In contrast, for the prismatic loading case the ductility drops sharply for  $W_0 \gtrsim 1/6$  but is independent of  $W_0$  for more oblate voids. The deformation anisotropy of the lateral ligaments and the occurrence of strain localization in the yz-plane is also persistent, cf. Figs. 17(b), 17(e) ( $\mathcal{T}=1$ ) and Figs. 17(c), 17(f) ( $\mathcal{T}=3$ ).

At  $\mathcal{T}=3$  (Fig. 16(c)), the regimes where the ductility is relatively insensitive to void shape  $(0 \leq \ln(1/W_0) \leq 2$  for  $\langle c \rangle$ -loading and  $2 \leq \ln(1/W_0) \leq 3.5$  for prismatic  $\langle a \rangle$ -loading) are also the regimes where extension twinning is more profuse in both loading orientations. In fact, the level of twinning in these regimes is nearly the same for both the orientations (cf. Figs. 7(h) and 14(d)).

#### 4. Discussion

The prismatic and  $\langle c \rangle$ -axis orientations considered in this work may be viewed as highly idealized representations of textured polycrystalline materials. For example, in technologically important HCP materials such as rolled polycrystalline Mg alloys, experiments are commonly performed along the rolling or transverse orientations which, roughly equate to the prismatic loading in our case in terms of the important deformation mechanisms. The other, relatively much less explored, extreme situation is the short-transverse orientation (Kondori et al., 2019), which is mimicked by the  $\langle c \rangle$ -axis loading in this work. In these materials, void nucleation is often reported at twin boundaries, twin–grain boundary intersections, or subsequent to the cracking of second phase particles (Kondori and Benzerga, 2017; Kondori et al., 2018; Azghandi et al., 2020b). Often, these second-phase particles are aligned with a material principal direction (Li et al., 2012; Ray and Wilkinson, 2016), which can set up initial conditions analogous to the unit cell representations in this work. Moreover, twin-induced penny-shaped voids (or cracks) are often perpendicular to the main loading direction (Kondori and Benzerga, 2014; Basu et al., 2017). In such situations, the nascent void can be approximated as oblate with a periodic distribution.

In this work, we analyzed the subsequent growth to coalescence of such initially oblate voids with varying aspect ratios. The relatively high value of the initial porosity is representative of locally attainable values. Despite the initial symmetry of the unit cell with regards to the geometry and loading ( $\Sigma_{xx} = \Sigma_{zz}$ ), a three-dimensional analysis is necessary because of the symmetry-breaking deformation anisotropy in the lateral plane for both, prismatic and  $\langle c \rangle$ -axis loading. With these considerations, we put the results in the context of relevant experimental observations and recent analyses.

Under uniaxial loading a wide spectrum of results are obtained depending on the aspect ratio of the initial void, Figs. 2 and 8. For instance, there seems to be a critical void aspect ratio below which porosity growth is unbounded, leading to failure, cf. Figs. 2(b) and 8(b). Such trends may depend on constitutive parameters. Song and Castañeda (2017c) indicate that at low triaxiality levels ( $\mathcal{T} \ll 1$ ) void shape plays a negligible role in void aspect ratio evolution but becomes important at  $\mathcal{T} \gtrsim 1$ . Our calculations

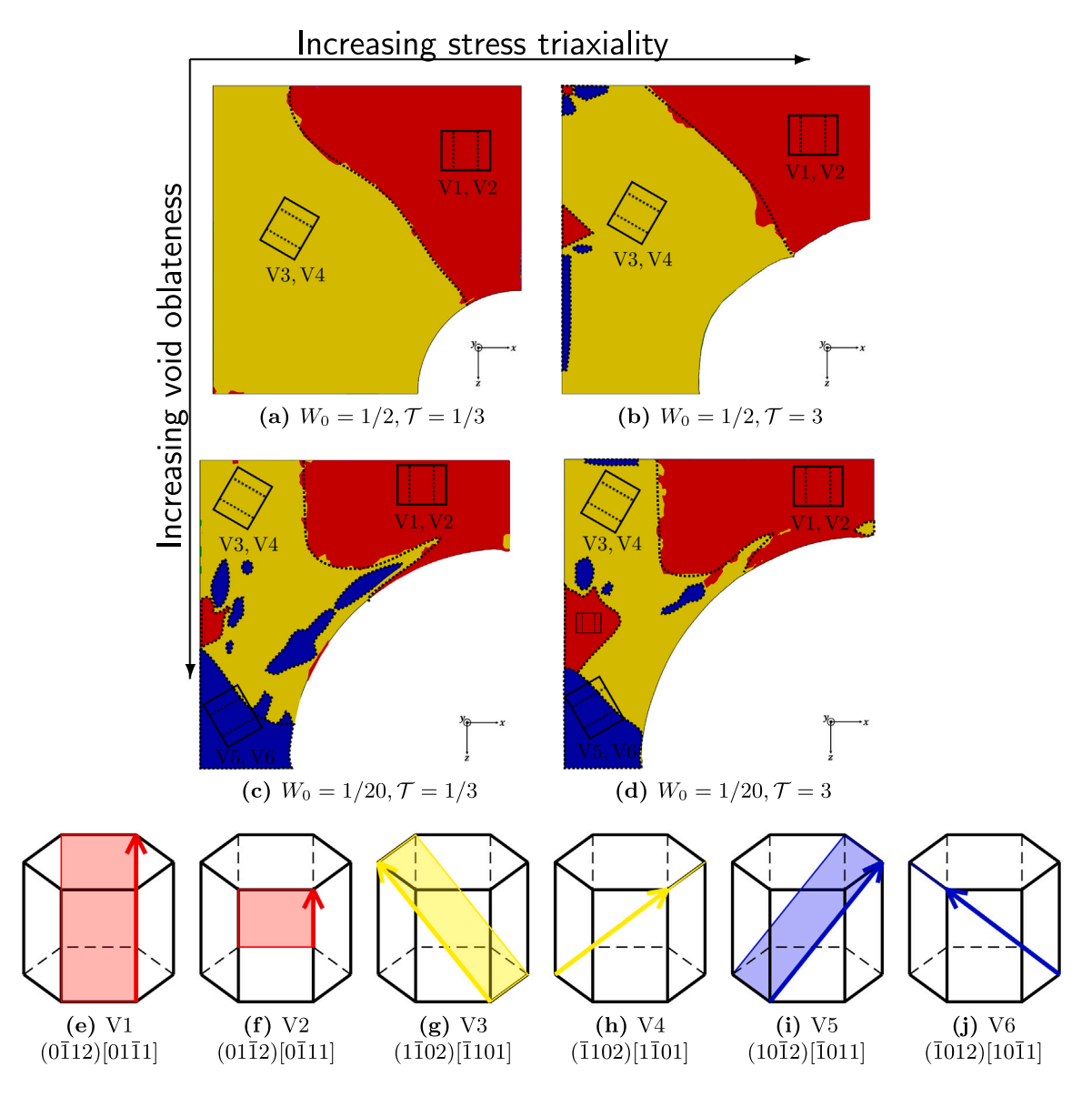


Fig. 15.  $\langle c \rangle$ -axis loading: Effect of void oblateness and triaxiality on the formation of twinned sectors around the void is shown in panels (a)–(d). The section is taken on the equatorial xz plane. The contours are shown at  $E_{eq} \sim 0.065$ . The different ET variants V1–V6 are schematically shown in panels (e)–(j). Twin sector boundaries marked by .... demarcate the different non-conjugate variants with a misorientation of  $\sim$ 60°.

reveal that void shape plays an important role in the evolution of W at all levels of  $\mathcal{T}$ . Crystallographic plastic anisotropy is found to dictate the rate of change of void aspect ratio ( $\dot{W}$ ). For porous  $J_2$  materials under uniaxial tension, penny-shaped voids tend to open up more rapidly along the loading direction compared to spherical voids (Pardoen and Hutchinson, 2000; Kweon et al., 2016), i.e.,  $\dot{W}_{\rm ob}/\dot{W}_{\rm sp} > 1$ . In contrast, we find that  $\dot{W}_{\rm ob}/\dot{W}_{\rm sp} < 1$  under prismatic (Fig. 2(c)) as well as  $\langle c \rangle$ -axis uniaxial tension (Fig. 8(c)). That is, oblate voids tend to open up slower than spherical ones. This observation is consistent with experimental measurements in some Mg alloys (Kondori and Benzerga, 2017). What is of particular importance is that the slow rate of opening of the voids is more damaging and leads to early coalescence. In the same work, Kondori and Benzerga (2017) show that this feature can be captured by heuristic modifications to micromechanical porous plasticity models (Keralavarma and Benzerga, 2010; Benzerga and Leblond, 2014), although the precise role of plastic anisotropy remains hidden. Our simulations reveal how the plastic anisotropy promotes lateral void growth, which can trigger failure. This provides a rationale for fracture under uniaxial loading, something that would not be observed for a  $J_2$  matrix under similar conditions.

In this regard, two aspects are particularly noteworthy, both pertaining to prismatic loading. First, for  $W_0 \lesssim 1/6$  the void aspect ratio is quasi-isotropic, but the ligament parameter ( $\chi$ ) evolution is anisotropic, cf. Fig. 2(d). This means that while the void grows nearly isotropically in the lateral directions (i.e.,  $r_x \approx r_z$ ), the cell boundaries move at different rates. In particular,  $L_x$  decreases

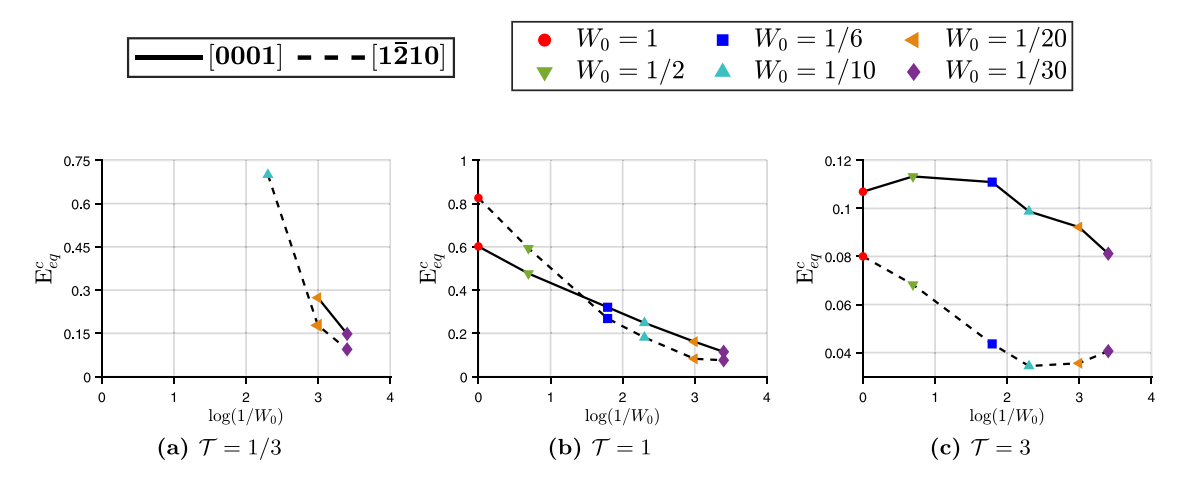


Fig. 16. Strain to failure,  $E_{\rho\rho}^c$ , versus  $\ln(1/W_0)$  prismatic loading (dashed) and c-axis loading (solid) and (a)  $\mathcal{T}=1/3$ , (b)  $\mathcal{T}=1$  and (c)  $\mathcal{T}=3$ .

much faster than  $L_z$ , which causes  $\chi_x > \chi_z$ . This suggests a propensity to directional coalescence, consistent with the experiments of Kondori et al. (2018). Second, prismatic loading exhibits a tendency for strain localization in shear bands under uniaxial (cf. Fig. 17(a)) and triaxial loading (Figs. 17(b)-17(c)), which supports macroscale observations (Benzerga et al., 2019). The same is not seen, however, under  $\langle c \rangle$ -axis loading (Figs. 17(d)-17(f)). These observations point to the subtle role of crystallographic plastic anisotropy in facilitating competing modes of failure.

Other recent uniaxial tensile experiments by Azghandi et al. (2020a) indicate that good ductility of a polycrystalline Mg alloy appears to correlate with reduced extension twinning that possibly assists in reduced void growth rates. While direct comparison is not possible, our simulations suggest that the correlation between twinning and failure is not straightforward. Consider the uniaxial tension results for  $W_0 = 1/20$ . The strain to failure is higher under  $\langle c \rangle$ -axis loading than it is under prismatic loading despite higher extension twinning activity in the former case. Correspondingly, porosity growth is also slower under  $\langle c \rangle$ -axis loading. Collating the trends from Figs. 16, 7(h) and 14(d), for the range of triaxialities the correlation between extension twinning and failure strain (at a given triaxiality level) with increasing oblateness is ostensibly the opposite for the two orientations. Under  $\langle c \rangle$ -axis loading, the decreasing ductility with increasing oblateness correlates with the decreasing twinning volume fraction, cf. Fig. 14(d). In contrast, under prismatic loading the decrease in ductility correlates with increased twinning activity over the same range of void aspect ratio, cf. Fig. 7(h). It may seem therefore that suppressing twinning may either be unfavorable ( $\langle c \rangle$ -axis loading) or favorable (prismatic loading) for ductility. However, another way to see this is that the void shape has a primary effect on ductility and a collateral effect on twinning rather than twinning playing a governing role in setting ductility limits.

The sensitivity of the stress-strain behavior to void oblateness for both orientations, see e.g., Figs. 3(a) and 10(a), is quite different from what is observed in power-law hardening materials (Keralavarma et al., 2011). Under sufficiently high triaxiality, the effective response is nearly independent of the crystallographic orientation. Under prismatic loading, triaxiality couples into the void oblateness effect to produce twinning-dominated responses that appear qualitatively similar to the  $\langle c \rangle$ -axis loading responses. Further, the average extension twin volume fractions in both cases are quite similar, cf. Figs. 7(h) and 14(d). In essence, it may be difficult to attribute a porous HCP material response to a particular loading orientation solely based on the stress-strain characteristics or even the twin volume fraction. To that end, the content and spatial distribution of the extension twin variants may serve as a better signature to interpret the orientation-triaxiality coupling as these are different for the two loading orientations (Indurkar et al., 2020), cf. Fig. 15. The increase in the number density of twin sectors with increasing void oblateness translates to an increased number density of high-angle sector boundaries, whose effect on final fracture modes can be crucial. Rodriguez et al. (2016) suggest that cracks appear in regions with lowest twin density while Prasad et al. (2015) suggest that twin boundaries may have a toughening effect via crack deflection. In our view, another factor that may be relevant is twin boundary misorientation, which depends on the number of activated twin variants in the matrix surrounding the void. The fracture characteristics may be complicated by the interplay between the amount of twinning and which twin variants are present. We speculate that the presence of twin variants with high misorientations may exacerbate final failure by causing strain localization or cracking along their sector boundaries, see for example Nemcko and Wilkinson (2016), Nemcko et al. (2016).

With these key findings, we comment on the prospects of formulating improved mechanism-based continuum models of HCP porous plasticity. A particularly important aspect is that inter-void ligament anisotropy may result from anisotropic evolution of the void shape or anisotropic evolution of the cell dimensions, which can cause anisotropic coalescence. While Morin et al. (2015) allows lateral void shape anisotropy it does not track cell anisotropy. Moreover, the evolution equations for the internal parameters characterizing the void shape and orientation are missing. The variational porous plasticity model by Song and Castañeda (2017a) incorporates evolving lateral void shape anisotropy but not cell anisotropy for tracking inter-void ligament evolution. The present unit cell results provide a basis to parametrize void shape and cell geometry evolution, both of which are important in predicting directional coalescence.

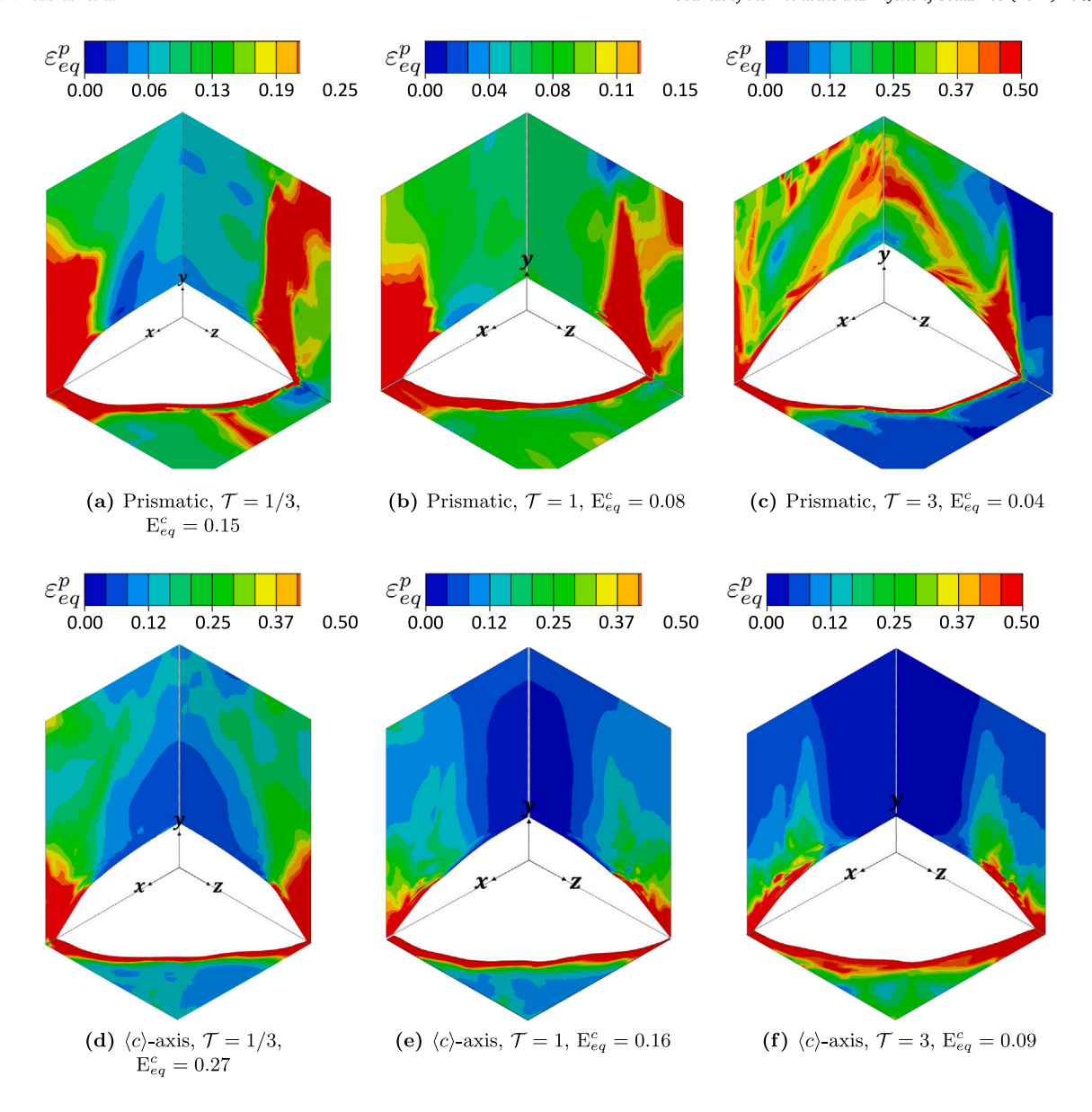


Fig. 17. Evolution of equivalent plastic strain  $\varepsilon_{eq}^p$  around a penny-shaped void ( $W_0 = 1/20$ ) at  $\mathcal{T} = 1/3$ , 1 and 3 for (a–c) prismatic loading, and (d–f)  $\langle c \rangle$ -axis loading.

Another aspect of crucial importance needed in crystallographically informed damage models (Ling et al., 2016; Paux et al., 2018; Song and Castañeda, 2017a,b) is the representation of twinning effects. A primary effect commonly associated with extension twinning is tension—compression asymmetry; porous plasticity models incorporating this feature (e.g., Stewart and Cazacu, 2011) assert its role in macroscale damage (Revil-Baudard et al., 2016). The present results emphasize that extension twinning goes beyond its expression in terms of tension—compression asymmetry. When coupled with void shape effects, it can fundamentally alter the micromechanical responses thereby setting up complex, and likely competing, scenarios for ultimate failure. It is important to incorporate such additional pathways for void evolution within homogenization based models.

## 5. Concluding remarks

In this work, we investigated the effect of void shape on the response of porous HCP single crystals under uniaxial and triaxial tensile stress states with magnesium as a model material. A primary focus is on understanding how slip and twinning mechanisms interact with the initially oblate voids that are often found to be the agents of ductile damage in such materials. Detailed analysis of the micro–macro linkages is performed for prismatic and  $\langle c \rangle$ -axis crystal orientations.

The key features that are common between spherical and oblate-voided responses are: (i) activation of extension twinning under prismatic loading, (ii) void-induced hardening for prismatic and  $\langle c \rangle$ -axis uniaxial loading for mildly oblate voids, and (iii) formation of extension twin sectors under  $\langle c \rangle$ -axis loading. Beyond these basic similarities, void shape plays a discernible role in the failure evolution in the presence of crystallographic plastic anisotropy and stress state.

- Oblate voids drive failure even under uniaxial stress states for both orientations. Crystallographic plastic anisotropy promotes lateral void growth (in the plane of coalescence), effectively resulting in flattened voids at coalescence.
- Under  $\langle c \rangle$ -axis uniaxial loading, the porosity evolution becomes increasingly non-monotonic with increasing oblateness.
- Void oblateness increases the propensity to anisotropic coalescence either via anisotropic void growth or via anisotropic cell deformation.
- At moderate to high triaxiality levels, void oblateness interacts with crystallographic plastic anisotropy, which leads to increased extension twinning for the prismatic orientation but decreased extension twinning for the  $\langle c \rangle$ -axis orientation.
- The distribution of twin variants around the void is more sensitive to void aspect ratio than the stress triaxiality. More oblate voids promote the formation of twin sector boundaries with high misorientation, which may play a role in premature failure.

Overall, the crystallographic plastic anisotropy of HCP materials and void aspect ratio interact to generate competing failure modes under tensile stress states, which includes void impingement via ligament necking, cracking along twin boundaries, and localization in shear bands.

This work focused on crystallographic orientations and loading states that result in an initially symmetric system. To gain further insights into porous HCP plasticity it is important to consider loading states and crystallographic orientations that are not symmetric. For instance, even under purely tensile loading states, small deviations from the two canonical orientations considered here would induce macroscopic shear deformations due to profuse basal slip. Likewise, even for symmetric initial orientations, a superimposed shear stress would result in complex porosity evolution. Such scenarios are complicated by the computational cost and the relatively large space of orientations and stress states that need to be considered. Investigating these aspects is underway.

### CRediT authorship contribution statement

**Padmeya P. Indurkar:** Conceptualization, Formal Analysis, Methodology, Writing – original draft, Writing – review & editing. **Shailendra P. Joshi:** Conceptualization, Methodology, Formal analysis, Writing – original draft, Writing – review & editing, Supervision, Funding acquisition. **A. Amine Benzerga:** Conceptualization, Writing – original draft, Writing – review & editing, Funding acquisition.

# Declaration of competing interest

The authors declare that they have no known competing financial interests or personal relationships that could have appeared to influence the work reported in this paper.

#### Acknowledgments

SPJ and AAB acknowledge support provided by the National Science Foundation, United States of America under: "Collaborative Research: Multiscale Modeling of Damage Tolerance in Hexagonal Materials" (Grant Numbers CMMI-1932976 to SPJ and CMMI-1932975 to AAB). PPI acknowledges partial support from NUS Research Scholarship, Singapore. PPI also acknowledges the funding support from Army Research Laboratory, United States of America under Cooperative Agreement Number W911NF-12-2-0022 and access to University of Houston computing facilities during his visit. The views and conclusions contained in this document are those of the authors and should not be interpreted as representing the official policies, either expressed or implied, of the Army Research Laboratory or the U.S. Government. The U.S. Government is authorized to reproduce and distribute reprints for Government purposes notwithstanding any copyright notation herein. The authors also acknowledge the use of the Opuntia and Carya clusters and the advanced support from the Research Computing Data Core at the University of Houston to carry out the research presented here.

# References

Agnew, S.R., Brown, D.W., Tomé, C.N., 2006. Validating a polycrystal model for the elastoplastic response of magnesium alloy AZ31 using in situ neutron diffraction. Acta Mater. 54 (18), 4841–4852. http://dx.doi.org/10.1016/j.actamat.2006.06.020, URL http://www.sciencedirect.com/science/article/pii/S1359645406004502.

Al-Samman, T., Gottstein, G., 2008. Room temperature formability of a magnesium AZ31 alloy: Examining the role of texture on the deformation mechanisms. Mater. Sci. Eng. A 488 (1), 406–414. http://dx.doi.org/10.1016/j.msea.2007.11.056, URL http://www.sciencedirect.com/science/article/pii/S0921509307018552.

Azghandi, SM, Weiss, M., Arhatari, BD, Adrien, J, Maire, E, Barnett, MR, 2020a. A rationale for the influence of grain size on failure of magnesium alloy AZ31:

An in situ X-ray microtomography study. Acta Mater. 200, 619–631.

Azghandi, S.H.M, Weiss, M., Arhatari, B.D., Barnett, M.R., 2020b. Grain size and void formation in Mg alloy AZ31. J. Alloys Compd. 816, 152618. Barnett, M.R., 2007a. Twinning and the ductility of magnesium alloys: Part II. "contraction" twins. Mater. Sci. Eng. A 464 (1), 8–16.

Barnett, M.R., 2007b. Twinning and the ductility of magnesium alloys: Part I:"tension" twins. Mater. Sci. Eng. A 464 (1), 1-7.

Basu, S., Dogan, E., Kondori, B., Karaman, I., Benzerga, A.A., 2017. Towards designing anisotropy for ductility enhancement: A theory-driven investigation in mg-alloys. Acta Mater. 131, 349–362. http://dx.doi.org/10.1016/j.actamat.2017.02.046, URL http://www.sciencedirect.com/science/article/pii/S1359645417301374

Becker, R., Lloyd, J.T., 2016. A reduced-order crystal model for HCP metals: application to Mg. Mech. Mater. 98, 98-110.

Benzerga, A.A., Besson, J., 2001. Plastic potentials for anisotropic porous solids. Eur. J. Mech. A Solids 20 (3), 397-434.

Benzerga, A.A., Leblond, J-B, 2014. Effective yield criterion accounting for microvoid coalescence. J. Appl. Mech. 81 (3), 031009.

Benzerga, A.A., Thomas, N., Herrington, J.S., 2019. Plastic flow anisotropy drives shear fracture. Sci. Rep. 9 (1), 1425.

Beyerlein, I.J., Tomé, C.N., 2008. A dislocation-based constitutive law for pure Zr including temperature effects. Int. J. Plast. 24 (5), 867–895. http://dx.doi.org/10.1016/j.iiplas.2007.07.017, URL http://www.sciencedirect.com/science/article/pii/S074964190700109X.

Bhattacharyya, J.J., Wang, F., McQuade, P.J., Agnew, S.R., 2017. Deformation and fracture behavior of Mg alloy, WE43, after various aging heat treatments. Mater. Sci. Eng. A 705, 79–88. http://dx.doi.org/10.1016/j.msea.2017.08.067, URL http://www.sciencedirect.com/science/article/pii/S0921509317310821. Cheng, J., Ghosh, S., 2017. Crystal plasticity finite element modeling of discrete twin evolution in polycrystalline magnesium. J. Mech. Phys. Solids 99, 512–538.

Friedrich, H., Schumann, S., 2001. Research for a "new age of magnesium" in the automotive industry. J. Mater Process. Technol. 117 (3), 276–281. http://dx.doi.org/10.1016/S0924-0136(01)00780-4, URL http://www.sciencedirect.com/science/article/pii/S0924013601007804.

Gan, Y.X., Kysar, J.W., 2007. Cylindrical void in a rigid-ideally plastic single crystal III: Hexagonal close-packed crystal. Int. J. Plast. 23 (4), 592-619.

Ha, S., Kim, K., 2010. Void growth and coalescence in f.c.c. single crystals. Int. J. Mech. Sci. 52 (7), 863–873. http://dx.doi.org/10.1016/j.ijmecsci.2010.03.001, URL http://www.sciencedirect.com/science/article/pii/S0020740310000445.

Han, X., Besson, J., Forest, S., Tanguy, B., Bugat, S., 2013. A yield function for single crystals containing voids. Int. J. Solids Struct. 50 (14), 2115-2131.

Hori, M., Nemat-Nasser, S., 1988. Mechanics of void growth and void collapse in crystals. Mech. Mater. 7 (1), 1-13.

Indurkar, P.P., 2020. On the multiscale mechanics of deformation, stability and damage in magnesium. (Ph.D. thesis). National University of Singapore.

Indurkar, P.P., Baweja, S., Perez, R., Joshi, S.P., 2020. Predicting textural variability effects in the anisotropic plasticity and stability of hexagonal metals: Application to magnesium and its alloys. Int. J. Plast. 102762. http://dx.doi.org/10.1016/j.ijplas.2020.102762, URL http://www.sciencedirect.com/science/article/pii/S0749641919309325.

Joshi, K., Joshi, S.P., 2022. On the micromechanics of voids in nanotwinned materials. J. Mech. Phys. Solids Accepted for Publication.

Kale, C., Rajagopalan, M., Turnage, S., Hornbuckle, B., Darling, K., Mathaudhu, S.N., Solanki, K.N., 2018. On the roles of stress-triaxiality and strain-rate on the deformation behavior of AZ31 magnesium alloys. Mater. Res. Lett. 6 (2), 152–158.

Kalidindi, S.R., 1998. Incorporation of deformation twinning in crystal plasticity models. J. Mech. Phys. Solids 46 (2), 267-290.

Kaushik, V., Narasimhan, R., Mishra, R.K., 2014. Experimental study of fracture behavior of magnesium single crystals. Mater. Sci. Eng. A 590, 174-185.

Kelley, E.W., Hosford, W.F., 1967. The plastic deformation of magnesium: technical report.

Keralavarma, S.M., Benzerga, A.A., 2010. A constitutive model for plastically anisotropic solids with non-spherical voids. J. Mech. Phys. Solids 58 (6), 874–901.

Keralavarma, S.M., Hoelscher, S., Benzerga, A.A., 2011. Void growth and coalescence in anisotropic plastic solids. Int. J. Solids Struct. 48 (11), 1696–1710.

Koike, J., 2005. Enhanced deformation mechanisms by anisotropic plasticity in polycrystalline mg alloys at room temperature. Metall. Mater. Trans. A 36 (7), 1689–1696. http://dx.doi.org/10.1007/s11661-005-0032-4.

Kondori, B., Benzerga, A.A., 2014. Effect of stress triaxiality on the flow and fracture of Mg alloy AZ31. Metall. Mater. Trans. A 45 (8), 3292–3307. http://dx.doi.org/10.1007/s11661-014-2211-7.

Kondori, B., Benzerga, A.A., 2015. On the notch ductility of a magnesium-rare earth alloy. Mater. Sci. Eng. A 647, 74-83.

Kondori, B., Benzerga, A.A., 2017. Modeling damage accumulation to fracture in a magnesium-rare earth alloy. Acta Mater. 124, 225-236.

Kondori, B., Madi, Y., Besson, J., Benzerga, A.A., 2019. Evolution of the 3D plastic anisotropy of HCP metals: experiments and modeling. 117, 71–92. http://dx.doi.org/10.1016/j.ijplas.2017.12.002.

Kondori, B., Morgeneyer, T.F., Helfen, L., Benzerga, A.A., 2018. Void growth and coalescence in a magnesium alloy studied by synchrotron radiation laminography. Acta Mater. 155, 80–94.

Koplik, J., Needleman, A., 1988. Void growth and coalescence in porous plastic solids. Int. J. Solids Struct. 24 (8), 835-853.

Kweon, S., Sagsoy, B., Benzerga, A.A., 2016. Constitutive relations and their time integration for anisotropic elasto-plastic porous materials. Comput. Methods Appl. Mech. Engrg. 310, 495-534.

Kysar, J.W., Gan, Y.X., Mendez-Arzuza, G., 2005. Cylindrical void in a rigid-ideally plastic single crystal. Part I: Anisotropic slip line theory solution for face-centered cubic crystals. Int. J. Plast. 21 (8), 1481–1520.

Lassance, D., Scheyvaerts, F., Pardoen, T., 2006. Growth and coalescence of penny-shaped voids in metallic alloys. Eng. Fract. Mech. 73 (8), 1009–1034. http://dx.doi.org/10.1016/j.engfracmech.2005.12.004, URL http://www.sciencedirect.com/science/article/pii/S0013794405003048.

Lee, M.G., Wagoner, R.H., Lee, J.K., Chung, K., Kim, H.Y., 2008. Constitutive modeling for anisotropic/asymmetric hardening behavior of magnesium alloy sheets. Int. J. Plast. 24 (4), 545–582.

Li, B., Joshi, S.P., Almagri, O., Ma, Q., Ramesh, K.T., Mukai, T., 2012. Rate-dependent hardening due to twinning in an ultrafine-grained magnesium alloy. Acta Mater. 60 (4), 1818–1826. http://dx.doi.org/10.1016/j.actamat.2011.12.002, URL http://www.sciencedirect.com/science/article/pii/S1359645411008640.

Ling, C., Besson, J., Forest, S., Tanguy, B., Latourte, F., Bosso, E., 2016. An elastoviscoplastic model for porous single crystals at finite strains and its assessment based on unit cell simulations. Int. J. Plast. 84, 58–87.

Lugo, M., Tschopp, M.A., Jordon, J.B., Horstemeyer, M.F., 2011. Microstructure and damage evolution during tensile loading in a wrought magnesium alloy. Scr. Mater. 64 (9), 912–915. http://dx.doi.org/10.1016/j.scriptamat.2011.01.029, URL http://www.sciencedirect.com/science/article/pii/S1359646211000406.

Mbiakop, A., Constantinescu, A., Danas, K., 2015a. An analytical model for porous single crystals with ellipsoidal voids. J. Mech. Phys. Solids 84, 436-467.

Mbiakop, A., Constantinescu, A., Danas, K., 2015b. A model for porous single crystals with cylindrical voids of elliptical cross-section. Int. J. Solids Struct. 64, 100–119.

Mordike, B.L, Ebert, T., 2001. Magnesium: Properties — applications — potential. Mater. Sci. Eng. A 302 (1), 37–45. http://dx.doi.org/10.1016/S0921-5093(00)01351-4, URL http://www.sciencedirect.com/science/article/pii/S0921509300013514.

Morin, L., Leblond, J.-B., Kondo, D., 2015. A gurson-type criterion for plastically anisotropic solids containing arbitrary ellipsoidal voids. Int. J. Solids Struct. 77, 86–101.

Nemcko, M.J., Li, J., Wilkinson, D.S., 2016. Effects of void band orientation and crystallographic anisotropy on void growth and coalescence. J. Mech. Phys. Solids 95, 270–283.

Nemcko, M.J., Wilkinson, D.S., 2016. Impact of microstructure on void growth and linkage in pure magnesium. Int. J. Fract. 200 (1-2), 31-47.

Pardoen, T., Hutchinson, J.W., 2000. An extended model for void growth and coalescence. J. Mech. Phys. Solids 48 (12), 2467-2512.

Paux, J., Brenner, R., Kondo, D., 2018. Plastic yield criterion and hardening of porous single crystals. Int. J. Solids Struct. 132, 80-95.

Paux, J., Morin, L., Brenner, R., Kondo, D., 2015. An approximate yield criterion for porous single crystals. Eur. J. Mech. A Solids 51, 1–10.

Pineau, A., Benzerga, A.A., Pardoen, T., 2016. Failure of metals I: Brittle and ductile fracture. Acta Mater. 107, 424-483.

Plunkett, B., Cazacu, O., Barlat, F., 2008. Orthotropic yield criteria for description of the anisotropy in tension and compression of sheet metals. Int. J. Plast. 24 (5), 847–866.

Potirniche, G.P., Hearndon, J.L., Horstemeyer, M.F., Ling, X.W., 2006. Lattice orientation effects on void growth and coalescence in fcc single crystals. Int. J. Plast. 22 (5), 921–942. http://dx.doi.org/10.1016/j.ijplas.2005.06.003, URL http://www.sciencedirect.com/science/article/pii/S0749641905001245.

Prasad, N.S., Narasimhan, R., Suwas, S., 2016. Numerical simulations of cylindrical void growth in Mg single crystals. Int. J. Fract. 200 (1-2), 159-183.

- Prasad, N.S., Narasimhan, R., Suwas, S., 2018. Effect of notch acuity on the fracture behavior of AZ31 Mg alloy. Eng. Fract. Mech. 187, 241-261.
- Prasad, N.S., Naveen Kumar, N., Narasimhan, R., Suwas, S., 2015. Fracture behavior of magnesium alloys role of tensile twinning. Acta Mater. 94, 281-293.
- Ray, A.K., Wilkinson, D.S., 2016. The effect of microstructure on damage and fracture in AZ31B and ZEK100 magnesium alloys. Mater. Sci. Eng. A 658, 33–41. Revil-Baudard, B., Cazacu, O., Flater, P., Chandola, N., Alves, J.L., 2016. Unusual plastic deformation and damage features in titanium: Experimental tests and constitutive modeling. J. Mech. Phys. Solids 88, 100–122.
- Rodriguez, A.K., Ayoub, G.A., Mansoor, B., Benzerga, A.A., 2016. Effect of strain rate and temperature on fracture of magnesium alloy AZ31B. Acta Mater. 112, 194-208
- Selvarajou, B., Joshi, S.P., Benzerga, A.A., 2017. Three dimensional simulations of texture and triaxiality effects on the plasticity of magnesium alloys. Acta Mater. 127, 54-72.
- Selvarajou, B., Joshi, S.P., Benzerga, A.A., 2019. Void growth and coalescence in hexagonal close packed crystals. J. Mech. Phys. Solids 125, 198-224.
- Selvarajou, B., Kondori, B., Benzerga, A.A., Joshi, S.P., 2016. On plastic flow in notched hexagonal close packed single crystals. J. Mech. Phys. Solids 94, 273–297. Somekawa, H., Singh, A., Mukai, T., 2009. Fracture mechanism of a coarse-grained magnesium alloy during fracture toughness testing. Phil. Mag. Lett. 89 (1), 2–10.
- Song, D., Castañeda, P.P., 2017a. A finite-strain homogenization model for viscoplastic porous single crystals: I-theory. J. Mech. Phys. Solids 107, 560-579.
- Song, D., Castañeda, P.P., 2017b. A finite-strain homogenization model for viscoplastic porous single crystals: II-applications. J. Mech. Phys. Solids 107, 580-602.
- Song, D., Castañeda, P.P., 2017c. Macroscopic response of strongly anisotropic porous viscoplastic single crystals and applications to ice. Extrem. Mech. Lett. 10, 41–49.
- Srivastava, A., Needleman, A., 2013. Void growth versus void collapse in a creeping single crystal. J. Mech. Phys. Solids 61 (5), 1169-1184.
- Srivastava, A., Needleman, A., 2015. Effect of crystal orientation on porosity evolution in a creeping single crystal. Mech. Mater. 90, 10-29.
- Steglich, D., Morgeneyer, T.F., 2013. Failure of magnesium sheets under monotonic loading: 3D examination of fracture mode and mechanisms. Int. J. Fract. 183 (1), 105–112. http://dx.doi.org/10.1007/s10704-013-9863-y.
- Stewart, J.B., Cazacu, O., 2011. Analytical yield criterion for an anisotropic material containing spherical voids and exhibiting tension-compression asymmetry. Int. J. Solids Struct. 48 (2), 357–373.
- Tekoglu, C., Leblond, J.-B., Pardoen, T., 2012. A criterion for the onset of void coalescence under combined tension and shear. J. Mech. Phys. Solids 60 (7), 1363–1381.
- Wang, H., Wu, P.D., Tomé, C.N., Wang, J., 2012. A constitutive model of twinning and detwinning for hexagonal close packed polycrystals. Mater. Sci. Eng. A 555, 93–98. http://dx.doi.org/10.1016/j.msea.2012.06.038, URL http://www.sciencedirect.com/science/article/pii/S0921509312008635.
- Yang, Q., Ghosh, S., 2022. A crystal plasticity model for porous HCP crystals in titanium alloys under multiaxial loading conditions. Int. J. Solids Struct. 238,
- Yerra, S.K., Tekoglu, C., Scheyvaerts, F., Delannay, L., Van Houtte, P., Pardoen, T., et al., 2010. Void growth and coalescence in single crystals. Int. J. Solids Struct. 47 (7-8), 1016-1029.
- Zhang, J., Joshi, S.P., 2012. Phenomenological crystal plasticity modeling and detailed micromechanical investigations of pure magnesium. J. Mech. Phys. Solids 60 (5), 945–972.
- Zhang, E., Yin, D., Xu, L., Yang, L., Yang, K., 2009. Microstructure, mechanical and corrosion properties and biocompatibility of Mg—Zn—Mn alloys for biomedical application. Mater. Sci. Eng. C 29 (3), 987–993. http://dx.doi.org/10.1016/j.msec.2008.08.024, URL http://www.sciencedirect.com/science/article/pii/S0928493108002117.